

CHAPTER 4

ELECTRONIC SPECTROSCOPIES

by Bert M. Weckhuysen and Robert A. Schoonheydt*

*Centrum voor Oppervlaktechemie en Katalyse,
Departement Interfasechemie, K.U.Leuven,
Kardinaal Mercierlaan 92, 3001 Leuven, Belgium*

Diffuse reflectance spectroscopy (DRS) in the ultraviolet, visible and near-infrared region is a versatile spectroscopic technique, as both d-d and charge transfer transitions of supported TMI can be probed. One of the advantages of electronic spectroscopy is that the obtained information is directly chemical since the outer shell electrons of the TMI are probed and provide information about the oxidation state and coordination environment of TMI on surfaces. Furthermore, the DRS technique can be used under *in situ* conditions and is quantitative under well-defined conditions. The main disadvantage is that diffuse reflectance spectra are complex, and usually encompasses several broad and overlapping bands. To avoid biased spectral analysis, chemometrical techniques need to be employed.

The chapter starts with a short overview of the principles of DRS spectroscopy. In the first two sections, theoretical and practical aspects of DRS, together with an introduction to crystal field, ligand field and molecular orbital theory are given. The third section will focus on selected examples in order to illustrate the potential and limitations of DRS spectroscopy for unravelling the chemistry of TMI on surfaces.

* Financial support for the research discussed in this chapter came from the Fonds voor Wetenschappelijk Onderzoek-Vlaanderen (FWO), the Geconcerteerde Onderzoeksactie (GOA) and the Inter-Universitaire Attractiepolen (IUAP). BMW thanks the FWO for a position as postdoctoral research fellow.

4.1. General principles of diffuse reflectance spectroscopy

The interaction of light in the near infrared (NIR), visible (Vis) and ultraviolet (UV) region with solids is a major tool in catalyst characterization. On such materials severe problems may arise due to light scattering phenomena. They are largely overcome by the application of techniques such as diffuse reflectance spectroscopy (DRS) and photoacoustic spectroscopy (PAS). Both methods have already been briefly discussed in Chapter III for measuring infrared spectra of solids, and a detailed account on DRS will be given in this chapter. The technique of PAS will not be treated because its use is rather limited. For detailed explanations and discussions-in-depth about DRS, we refer to the book of Kortüm [1] and to several review papers [2-5].

4.1.1. Light scattering and the Schuster-Kubelka-Munk theory

DRS is based on the reflection of light by a powdered sample, and the dimensions of the individual particles in such powdered sample are comparable to the wavelength; *i.e.*, 0.2-3 μ . This makes it impossible to distinguish the phenomena of reflection, refraction and diffraction; the light is scattered. There are two extreme situations of reflection: specular and diffuse reflection (Figure IV.1). In the case of specular reflection from a smooth and nonabsorbing medium, the light beam is reflected under the same angle by the surface as that of the incoming light beam. On the other hand, diffuse reflected light from a nonabsorbing medium involves photons, which are scattered in all directions. Three different regimes can be distinguished: (1) single scattering; (2) multiple scattering and (3) dependent scattering (Figure IV.2). The first type arises when scattering centers are sufficiently apart that each is illuminated only by photons not previously scattered, and on the average, there is no phase relationship between the photons scattered from neighbouring particles. In the case of multiple scattering, the scattering centers are still far enough apart that they may be treated as independent but each is now illuminated by photons scattered from adjacent particles.

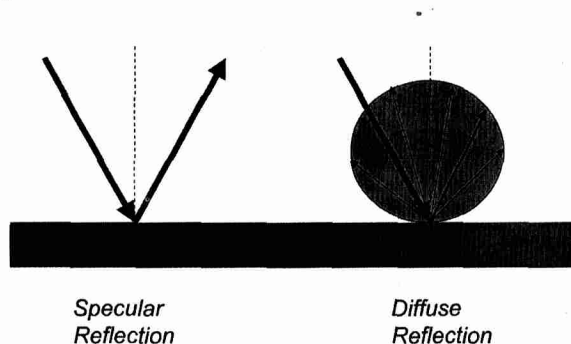


Figure IV.1. Light scattering at smooth nonabsorbing surfaces: specular and diffuse reflection.

Dependent scattering arises when, in addition to multiple scattering, phase coherence exists between scattered photons from adjacent centers. As a rule of thumb, one can say that dependent scattering is present, if the average distance (d) between scattering centers is less than three times the particle diameter ($3D$) (Figure IV.2).

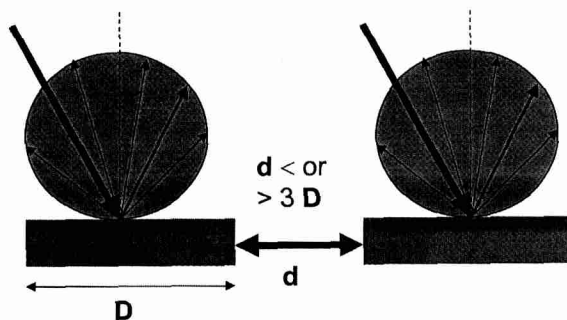


Figure IV.2. Rule of thumb discriminating between single, multiple and dependent scattering.

The division of light scattering systems into the above three regimes determines the theoretical approach necessary to describe the scattered light intensity. For single and multiple scattering, the absence of phase coherence ensures that the total scattered light intensity is merely the sum of the intensities of the individual scatterers. Both type of scattering can be mathematically treated in a rather easy way. In contrast, when the particles become so tightly packed that phase coherence becomes important, amplitudes rather than intensities must be summed. This is the case for heterogeneous catalysts because they are always investigated in the form of densely packed powders. Then, the Radiative Transfer Theory has to be called in, which sets out to solve the Radiative Transfer Equation:

$$\frac{-dI}{\kappa \cdot \rho \cdot dS} = I \frac{j}{\kappa} \quad (\text{Eq. IV.1})$$

with I , the incident light intensity of a given wavelength; dI/dS , the change of the intensity with the pathlength dS ; ρ , the density of the medium; κ , an attenuation coefficient corresponding with the total radiation loss due to absorption and scattering and j , the scattering coefficient, which is defined through the function $j(\theta, \phi)$:

$$j(\theta, \phi) = \frac{\kappa}{4\pi} \int_0^{\pi} \int_0^{2\pi} p(\theta, \phi; \theta', \phi') I(\theta', \phi') \sin \theta' d\theta' d\phi' \quad (\text{Eq. IV.2})$$

Eq. IV.1, which is schematically illustrated in Figure IV.3, can be solved by introducing simplifications which are related with easily attainable experimental conditions. These ideas, first suggested by Schuster and later on further developed by

Kubelka and Munk, simplify the solution of the radiative transfer equation (Eq. IV.1), known as the Schuster-Kubelka-Munk (S-K-M) theory.

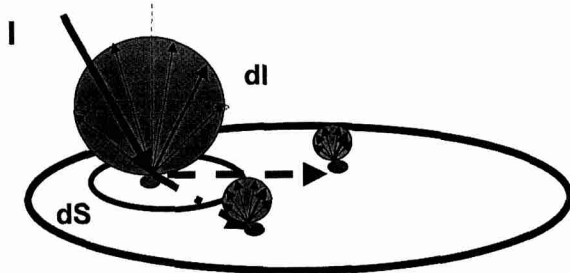


Figure IV.3. Scheme of dependent scattering.

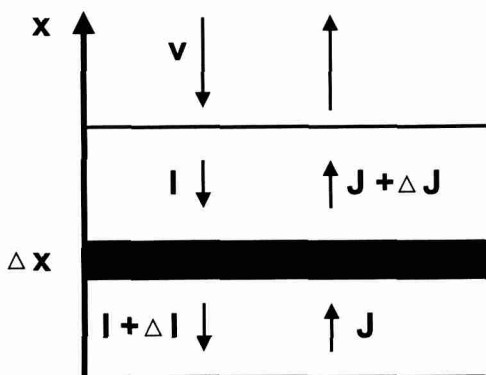


Figure IV.4. The Schuster-Kubelka-Munk approximation: the incident and remitted light fluxes are approximated by two opposite fluxes, perpendicular to the surface of the infinitely thick sample layer.

In this S-K-M theory, the incident and scattered light flux are approximated by two fluxes I and J , which are perpendicular to the surface of the powdered sample, but in opposite direction. This is illustrated in Fig. IV.4.. I is the flux of monochromatic diffuse illumination, whereas J is the flux of diffusively scattered light. If the sample is infinitely thick, the diffuse reflection of the sample (R_∞) is related to an apparent absorption (K) and apparent scattering coefficient (S) via the Schuster-Kubelka-Munk (S-K-M) or Kubelka-Munk (K-M) function:

$$F(R_\infty) = \frac{(1 - R_\infty)^2}{2R_\infty} = \frac{K}{S} \quad (\text{Eq. IV.3})$$

Eq. IV.3 is valid under the following conditions:

- (a) diffuse monochromatic irradiation of the powdered sample;
- (b) isotropic light scattering;
- (c) an infinite layer thickness;
- (d) a low concentration of absorbing centers;
- (e) a uniform distribution of absorbing centers;
- (f) the absence of fluorescence.

R_{∞} is experimentally measured as the light intensity reflected from the powdered sample divided by the light intensity reflected from an ideally white reference standard. K and S are characteristic of the sample under investigation, and the true absorption coefficient α_v and true scattering coefficient σ_v at frequency ν are related to K and S via:

$$\alpha_v = \eta \cdot K \text{ and } \sigma_v = \chi \cdot S \quad (\text{Eq. IV.4})$$

Values of η and χ are plotted and tabulated for a range of K/S values, and it is shown that in the limit of small absorptions η and χ are equal to $1/2$ and $4/3$, respectively.

It follows from (Eq. IV.3) and (Eq. IV.4) that:

$$\frac{\alpha_v}{\sigma_v} = \frac{(1 - R_{\infty})^2}{2R_{\infty}} \cdot \frac{\eta}{\chi} \quad (\text{Eq. IV.5})$$

Equations (Eq. IV.4) and (Eq. IV.5) are introduced by Klier [6], and the ratio η/χ is fairly constant and equal to $3/8$ for values of K/S between 0 and 0.3. For strongly absorbing solids ($K/S > 0.3$ or $R_{\infty} < 0.5$) η/χ decreases. Thus, at low concentrations of supported TMI, Eq. IV.3 is a good representation of the absorbing spectrum, and allows a quantitative determination of the TMI according to:

$$F(R_{\infty}) = \frac{(1 - R_{\infty})^2}{2R_{\infty}} = \frac{K}{S} = \frac{\alpha \cdot C_{\text{TMI}}}{S} = k \cdot C_{\text{TMI}} \quad (\text{Eq. IV.6})$$

When at a given wavelength λ , S is constant, Eq. IV.6 gives a linear relation between $F(R_{\infty})$ and the TMI concentration, C_{TMI} . The coefficients α and k are proportionality constants.

As mentioned above, the S-K-M equation is only valid under well-defined conditions. Conditions (a), (b) and (d) are most closely met when the medium consists of densely packed, randomly shaped particles containing low amounts of transition metal ions. The infinite thickness criterion (condition (c)) is usually reached for sample layers of 5 mm thickness, although supported metal oxide catalysts made from some silicas (e.g., *Cab-O-Sil* Cabot and *Aerosil* Degussa) may need thicker layers. For work in vacuum, adsorption studies or catalytic experiments specially designed cells are necessary with silica windows with extremely low OH and H_2O contents. It is also advisable to sieve the catalyst and to work with fractions of the same size range.

Finally, it is important to stress that the scattering power of a catalyst system, as expressed by S , is not of any importance provided that it is not a function of the wavelength. If S is wavelength dependent then distortions, appearing mostly as a smoothly shifting baseline, will result since K/S is measured as a function of ν .

Fortunately, a strong wavelength dependence of S is not expected for particles, which are large in comparison to the wavelength of the scattering radiation. Indeed, the wavelength dependence of S can be expressed as:

$$S = v^\alpha \quad (\text{Eq. IV.7})$$

Parameter α approaches 0 for particle sizes much larger than the wavelength. It is approximately 1 for particle sizes of the order of wavelength. It attains values between 2 and 4, increasing with decreasing particle size, which is in any case smaller than the wavelength. The situation $\alpha = 4$ corresponds to single scattering at small particles, and the equation is then similar to that what was derived in Chapter III for Raman spectroscopy.

4.1.2. Instrumentation

In a DRS spectrum the ratio of the light scattered from an infinitely thick layer and the scattered light from an ideal non-absorbing reference sample is measured as a function of the wavelength λ [7]. The illumination of powdered samples by incident radiation leads to diffuse illumination of the material. This incident light is then partially absorbed, partially scattered by the particles. All DRS spectrometers are classical double beam spectrometers with fully automated acquisition, background subtraction and file storage. This allows the user to calculate the S-K-M function according to Eq. IV.6, and to perform band decomposition routines and chemometrical analysis. The light sources are a D_2 lamp for UV irradiation and a Tungsten filament for the Vis-NIR region, while the reflected light is detected with a photomultiplier in the UV-Vis region, and a PbS detector in the NIR region. There are three different diffuse reflectance attachments currently commercially available:

(1) An integration sphere. This attachment collects all the light scattered from the catalyst sample and from a reference standard and the detectors are placed on top of the integration sphere. This is the classical set-up of a DRS spectrometer, which is illustrated in Figure IV.5. Because the integration sphere must scatter the light and not absorb it, it is coated with a perfectly white material (MgO, etc.). In this way, a negligibly small amount of specular reflection is included. This setup cannot be used for real *in situ* measurements, and requires special quartz cells for treating the catalyst at high temperatures in the absence or presence of reactive molecules in a separate furnace. Figure IV.6 illustrates two types of quartz cells currently in use in our laboratory for measurements of heterogeneous catalysts in the dehydrated state, after adsorption of probe molecules, etc. Type A allows pretreatment of the samples with the desired gas flow through the catalyst bed, whereas Type B is designed for measurements in vacuum or static atmospheres.

(2) A Praying Mantis diffuse reflectance attachment. An example of such a setup (Harrick) is shown in Figures IV.7 and IV.8 [8]. Its construction with two ellipsoidal

mirrors is such that mainly the diffuse component of the reflected light is captured. In conjunction with the Praying Mantis diffuse reflectance attachment a stainless steel reaction chamber can be used for either vacuum or low/high pressure *in situ* measurements. This system has three gas ports for evacuation of the chamber and/or for introducing gas, while the temperature near the catalyst bed can be controlled by an electronically steered heating system and circulating tap water for cooling the outer section of the reaction chamber. This chamber can thus be used under dynamic conditions and the gases can be *on line* analyzed by *e.g.* gas chromatography. It is also clear that this setup requires much less sample than the classical one (100 mg versus 2 g), and consequently, the pretreatment time can be drastically reduced. A disadvantage of such *in situ* DRS measurements is that mostly only the region between 300 and 800 nm can be measured because of the heat radiation in the NIR region and spectral noise in the 200-300 nm region.

(3) A Fiber Optics diffuse reflectance attachment. This attachment has a high-temperature optical fiber, which connects *e.g.* a catalytic reactor with an optical device replacing the classical integration sphere. Such set-up allows to perform *on line in situ* measurements of a real catalytic reactor, although - to the best of our knowledge - no scientific publications have appeared in the field of heterogeneous catalysis with this technique.

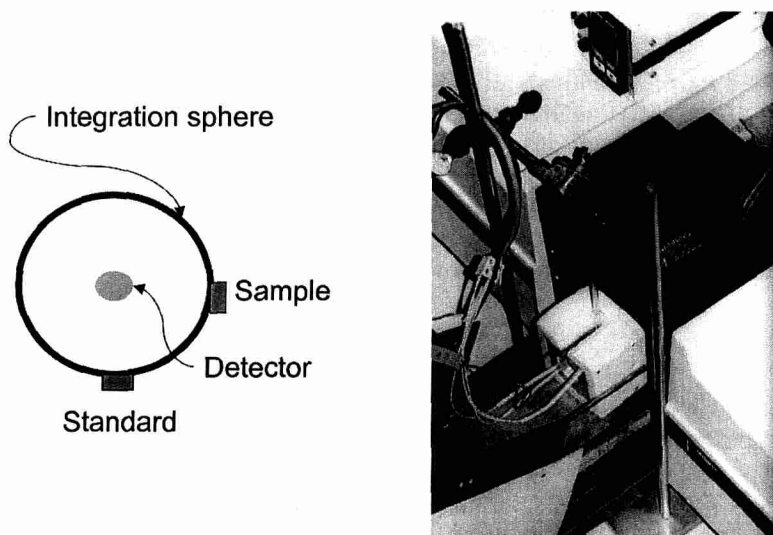


Figure IV.5. Schematic overview and picture of a diffuse reflectance spectrophotometer equipped with an integration sphere.

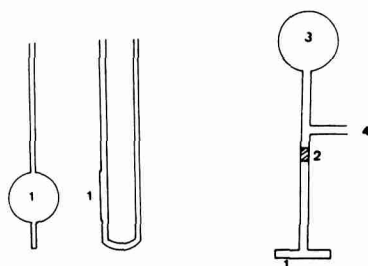


Figure IV.6. Quartz cells for DRS measurements using an intergration sphere: (1) suprasil; (2) quartz-Pyrex transitions; (3) pretreatment volumes; and (4) exit to vacuum line.

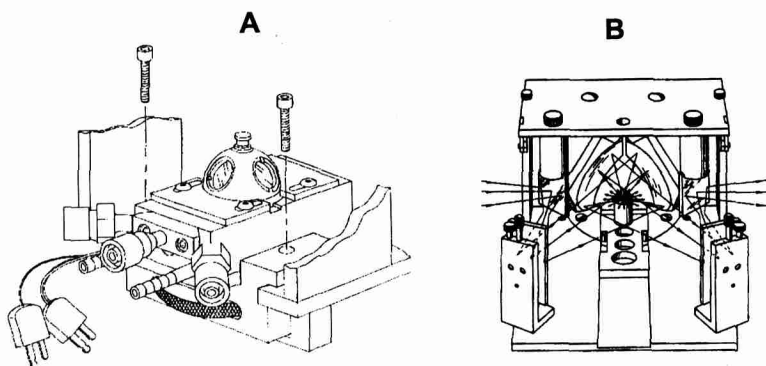


Figure IV.7. A Praying Mantis diffuse reflectance attachment for in situ DRS measurements: (A) Praying Mantis diffuse reflection attachment and (B) stainless steel reaction chamber.

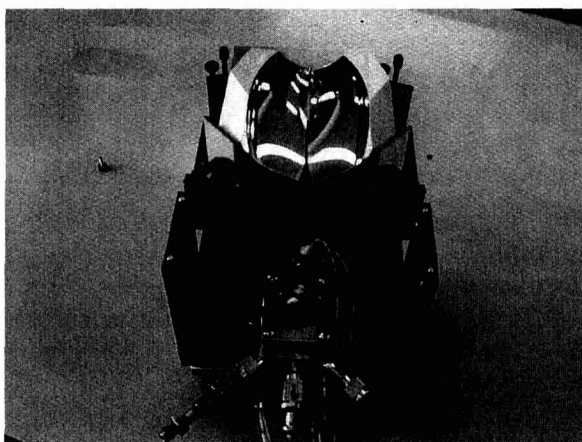


Figure IV.8. Picture of the Praying Mantis diffuse reflectance attachment used for in situ measurements.

The choice of a proper reference standard and coating material for the integration sphere is also crucial for reliable DRS measurements. Excellent reference materials are totally reflecting over an as wide as possible frequency range. In addition, they must be stable towards water and other chemical compounds. Indeed, the presence of contaminants may result in a decrease of the reflection in the NIR (*e.g.*, water), VIS (*e.g.*, chlorophyll) and UV (*e.g.*, aromatics) region. Nowadays, polytetrafluoroethylene (PTFE) is preferred over the more traditional reference materials (MgO and BaSO₄) because of its superior NIR performances. It is also important to notice that reference standards suffer from aging, and that they must be regularly checked, and, if necessary, replaced. An alternative way of working is to use the bare oxide support (*e.g.*, SiO₂, Al₂O₃, ZrO₂ and TiO₂) as a reference material. In this way, one can correct for the light absorption by the support, which may hamper the investigation of the supported TMI. This is especially important for TMIs with charge transfer transitions in the UV region (*e.g.*, Re⁷⁺). Furthermore, when the bare oxide support and supported metal oxide catalysts are studied in the same type of DRS cells, effects due to these DRS cells can be eliminated provided that the scattering properties of the material are not changed by loading the material with transition metal ions. There are some indications that this is not always the case especially in the UV region of the spectrum.

4.2. Chemical information from DRS

As was already mentioned before, DRS in the frequency range 5000 (NIR) to 50000 cm⁻¹ (UV) probes both the d-d transitions and charge transfer (CT) transitions of TMI. As a result, DRS can provide very useful information about the oxidation state and coordination environment of TMI on surfaces. The interpretation of these d-d and CT transitions requires background in crystal field, ligand field and molecular orbital theory. A brief introduction will be presented here, but for a detailed account we refer to several excellent textbooks [9-11].

4.2.1. Crystal field Theory

Crystal field (CF) theory describes the origins and consequences of interactions of the surroundings on the orbital energy levels of a TMI. These interactions are considered as purely electrostatic because of the attraction between a positively charged cation and a ligand, which - even if not actually having a net negative charge - at least presents a negative charge in the form of its lone-pair of electrons towards the cation. These ligands are treated as point negative charges situated at a distance equal to the ionic radius of the transition metal ion. The corresponding energy is the CF potential, which is equal to:

$$V(r_i) = \sum_{j=1}^n \frac{e^2}{|R_j - r_i|} \quad (\text{Eq. IV.8})$$

with R_j is the distance TMI nucleus-ligand j , r_i is the distance TMI nucleus-electron i , and n is the number of ligands. For m electrons the CF potential is then:

$$V_{CF} = \sum_{i=1}^m V(r_i) \quad (\text{Eq. IV.9})$$

4.2.1.1. Crystal field splitting

The effect of V_{CF} on the d orbitals is that all orbitals are destabilized, but – depending on their orientation in space – to a different degree. This effect is schematically illustrated for an octahedral crystal field in Figure IV.9. Such octahedral complex is formed by six ligands approaching the metal ion along the x -, y - and z -axis until they reach their equilibrium positions. As they approach, the electrons in the d orbitals will be repelled, and the energy of these orbitals will be increased. The $d_{x^2-y^2}$ and d_{z^2} orbitals, which point directly towards the ligands will be affected more than the d_{xy} , d_{yz} and d_{xz} orbitals, which point between the approaching ligands. The effect can be considered in two steps as shown in Figure IV.9. First, there is an average increase in the energy of the d orbitals, which is what would be observed if the d orbitals were individually spherically symmetrical and were affected identically. In a second step, the energies of the d orbitals split into two sets because two are axial and three are non-axial and so are affected by the ligands differently. Relative to the “average” energy, the axial orbitals (described as the e_g set) increase in energy, while the non-axial orbitals (described as the t_{2g} set) decrease in energy. Their separation is given the symbol Δ_o or $10Dq$, and called the crystal field splitting parameter.

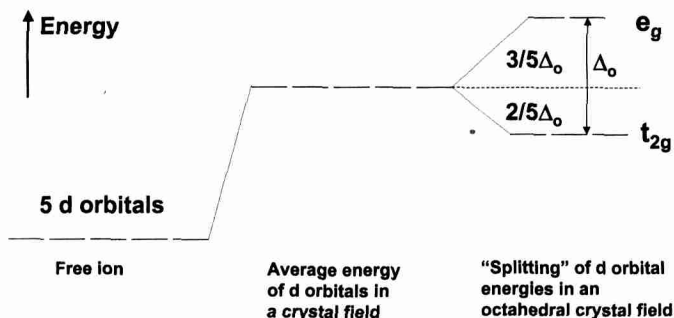


Figure IV.9. The effect of an octahedral crystal field on the d orbitals of a transition metal ion.

The separation in energy suggests that the electrons occupying the d -orbitals may rearrange. This rearrangement forms the basis of d - d spectra (crystal field spectra) or more generally electronic absorption spectra, although the latter also includes charge

transfer or interelectronic transitions between the TMI and the surrounding ligands (see further). Indeed, an electron in the t_{2g} set of the TMI can be excited to the e_g set by absorption of light with frequency ν according to $\Delta E = h\nu = 10Dq$.

Since energy is required to force two electrons to occupy a single d orbital, the electrons tend to remain unpaired in accordance with Hund's rules. However, they will also tend to occupy the d orbitals of lowest energy. If $10Dq$ is large enough then electrons which would otherwise remain unpaired in the e_g orbitals may instead be forced to pair in the lower t_{2g} orbitals. The energy required for such pairing is called the pairing energy P . This poses no problem for d^1 , d^2 and d^3 configurations (since the t_{2g} set remain degenerate) nor for d^8 and d^9 configurations in which electrons are necessarily paired in the t_{2g} set. But for the d^4 , d^5 , d^6 and d^7 configurations two possibilities arise depending on the magnitude of $10Dq$. If $10Dq$ is small (as compared with P) within one orbital; *i.e.*, the crystal field is weak, then the maximum possible number of electrons remains unpaired and the configurations are known as "high-spin". If $10Dq$ is large, that is the crystal field is strong, electrons are forced to pair in the lower t_{2g} set and the configurations are known as "low-spin". This is summarized in Figure IV.10. The crystal field stabilization energy (CFSE) is defined as the energy gain of the ground state of the TMI in the CF potential of its surrounding ligands with respect to their ground state energy in a spherical potential.

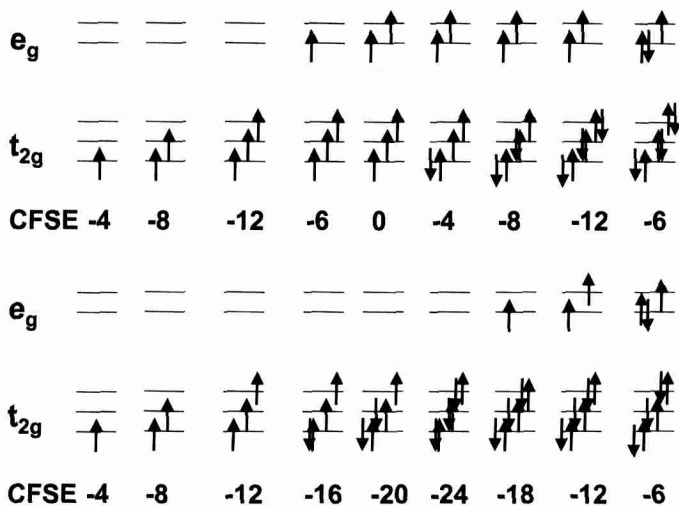


Figure IV.10. Arrangements of d electrons in weak (upper) and strong (lower) crystal fields. The corresponding crystal field stabilization energies are given in units of Dq . There, where electrons with anti-parallel spins are present this CFSE is counteracted by the electron pair repulsion energy times the number of electron pairs.

The formation of a tetrahedral complex can be imagined to occur in essentially the same way as described for the octahedral complex. This is illustrated in Figure

IV.11. Now, the $d_{x^2-y^2}$ and d_{z^2} orbitals will be less affected than the d_{xy} , d_{yz} and d_{xz} orbitals. The electrons in the t_2 level will be more strongly repelled than those in the e level. For the same TMI, ligands and metal-ligand distances, one can obtain that: $|\Delta_t| = \frac{4}{9} |\Delta_o|$. The occurrence of high- and low-spin configuration is again possible of d^3 , d^4 , d^5 and d^6 -ions, but in practice examples of low spin T_d are very rare because of the smaller $10Dq$ values involved.

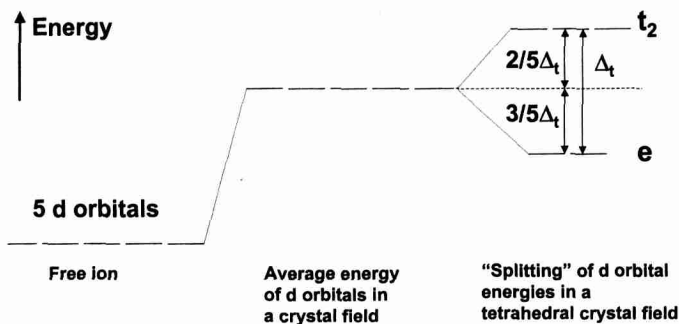


Figure IV.11. The effect of a tetrahedral crystal field on the d orbitals of a transition metal ion.

Besides octahedral and tetrahedral complexes, other coordination geometries may occur, and it is out of the scope of this chapter to give a detailed account for the effect of all coordination geometries on the energy levels of the d orbitals. A final example is given in Figure IV.12 for a square planar coordination. This four-coordinate complex can be described by a distorted octahedral complex in which the two *trans* ligands on the z -axis have been removed. This produces a great stabilization of the d_{z^2} orbital relative to the octahedral case. In addition, there is a small stabilization of the d_{xz} and d_{yz} orbital and, because of the loss of two ligands the remaining four ligands can move closer to the metal ion. The latter results in a destabilization of the $d_{x^2-y^2}$ and d_{xy} orbitals.

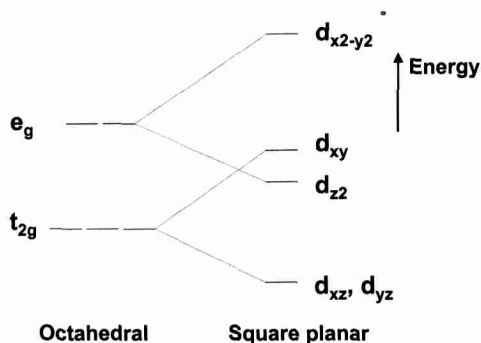


Figure IV.12. The effect of a square-planar crystal field on the d orbitals of a transition metal ion.

Besides coordination geometry around the TMI, other factors also influence the magnitude of the crystal field splitting parameter $10Dq$. These factors are:

1. Type of TMI: The values of $10Dq$ are generally higher for trivalent cations than for corresponding divalent cations. For example, $10Dq$ values for Fe^{2+} and Fe^{3+} in oxides are equal to 10,200 and 14,300 cm^{-1} , respectively. There is also a general sequence of $10Dq$ values, which increase in the order: $Mn^{2+} < Ni^{2+} < Co^{2+} < Fe^{2+} < V^{2+} < Fe^{3+} < Cr^{3+} < V^{3+} < Co^{3+} < Mn^{4+}$. Moreover, between successive transition metal ion series (1st row versus 2nd row TMI), values of $10Dq$ increase by about 30 to 50%.
2. Type of Ligand: Ligands coordinating to TMI may also be arranged in order of increasing $10Dq$ value. This order is called the spectrochemical series, reflecting colour variations in chemical compounds of transition metal ions with different ligands. Thus, for Cr^{3+} and Co^{2+} cations in octahedral coordination with different ligands, the order of increasing $10Dq$ value is: $I^- < Br^- < Cl^- < SCN^- < F^- < OH^- < oxalate^- < O^{2-} < H_2O < pyridine < NH_3 < ethylenediamine < SO_3^{2-} < NO_2^- < HS^- < S^{2-} < CN^-$. The ligands on the lefthand side of the series (starting from water) are called weak ligands because they result in weak crystal field strengths. The ligands on the righthand side (starting from water) are called strong ligands, and they will most probably form low spin complexes. This order is, of course, difficult to rationalize in terms of electrostatic energies as suggested by the point-charge model of CF theory. Therefore, other more refined theories have to be called in (see further).
3. Interatomic Distance: The value of $10Dq$ is inversely proportional with the fifth-power of the distance between the transition metal ion and the surrounding ligands ($1/R^5$), which indicates that $10Dq$ changes rapidly with small variations in R .

$$\frac{10Dq(T)}{10Dq(T_0)} = \left[\frac{V_{T_0}}{V_T} \right]^{\frac{5}{3}} \quad (Eq. IV.10)$$

4. Temperature: The temperature variation of $10Dq$ may be expressed by Eq. IV.10. Here, V_{T_0} and V_T are the molar volumes at room and elevated temperatures, respectively. Because mostly $V_{T_0} < V_T$, decreased $10Dq$ values are expected at higher temperatures. This observation is important for *in situ* DRS measurements at high temperatures. Other effect of high temperatures on the DRS spectra are illustrated in Figure IV.13. This figure shows the potential energy diagram of the ground and excited state, and the difference in width and the asymmetry of the spectral profiles at room and elevated temperatures. It is clear that absorption bands shift to lower energy, becomes more asymmetric and broader at higher temperatures.

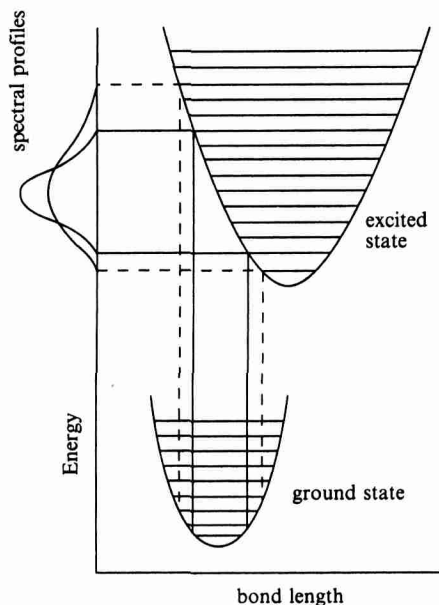


Figure IV.13. Potential energy diagram showing how an electronic transition takes place between the ground and excited state. The illustration also demonstrates how the width and asymmetry of an absorption band changes at higher temperature as a result of increased thermal population of vibrational levels of the ground electronic state. (After ref. [10].)

4.2.1.2. Spectroscopic terms and d-d transitions

Up to now, we have discussed the splitting diagrams for several coordination geometries assuming that all the rearrangements of electrons between the d orbitals with lower and higher energy are possible. This is not the case and we have in order to rationalize the d-d transitions to define the angular momentum of a multi-electron atom. This is characterized – in analogy with the quantum numbers l and m_s for an individual electron – by the quantum numbers L and S . The angular momenta associated with L and S are derived by the vectorial summation of the angular momenta associated with the l and m_s according to what is generally known as the Russell-Saunders or LS coupling scheme. A spectroscopic term is a conventional symbol used to specify a particular pair of L and S values, which defines the angular momentum. The ground term is the term, which describes the electronic arrangement of the atom, which has the lowest energy, and it is the action of the crystal field on this ground term, which is responsible for the observed d-d transitions.

The summations necessary to deduce the ground term can be explained as follows. The overall spin quantum number S is the sum of the spin quantum numbers of the individual electrons with $m_s = \pm \frac{1}{2}$; *i.e.*, S is equal to half the number of unpaired electrons. According to Hund's first rule, S takes the maximum value it can. The overall quantum number L is the sum of the magnetic quantum numbers

(m_l). Hund's second rule states that L will take the maximum value possible. The application of both rules is demonstrated in Figure IV.14 for a d^3 configuration (e.g., Cr^{3+}). Each box represents a d-orbital and is labelled with a m_l value. Both Hund's rules are then satisfied by filling these boxes singly from left to right, which results in $S = 3/2$ and $L = 3$. These values define the spectroscopic groundterm, which is equal to 4F . The number 4 represents the spin multiplicity ($2S + 1$), while the letter F arises from the value of L, which is defined in exactly the same way that the symbols for different values for l; i.e.,

S, P, D, F, ... correspond to $L = 0, 1, 2, 3, \dots$

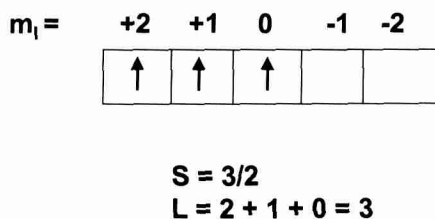


Figure IV.14. Coupling scheme for determining S and L for a d^3 configuration.

In this way, one can determine the ground terms for all d^n configurations. These are summarized in Table IV.1.

Table IV.1. Ground terms for d^n configurations.

n	1	2	3	4	5	6	7	8	9
Ground term	2D	3F	4F	5D	6S	5D	4F	3F	2D

Besides the spin multiplicity already noted, each of these terms has an orbital multiplicity of $2L+1$. This is analogous to the multiplicity $2l+1$, which tells us how many degenerate orbitals there are of a particular kind in a free ion; i.e., s, p, d or f. A crystal field imposed by the ligands lifts not only the degeneracy of the atomic orbitals, but also the orbital degeneracy of the ground terms and produces a number of component terms. This is shown for the different ground terms in Figure IV.15 for an octahedral coordination around the TMI. Here, the A term is an orbitally non-degenerate term, the E term is doubly degenerate and the T term is triply degenerate. In the case of Cr^{3+} (d^3), this leads to a splitting of the F ground term into three component terms T_{1g} , T_{2g} and A_{2g} , which has an overall orbital degeneracy of $3 + 3 + 1 = 7$, which is equal to the orbital multiplicity of $2L+1$ ($L = 3$).

An overview of the correlation of the spectroscopic ground terms with the electron configuration for d^n ions in an octahedral crystal field is given in Figure IV.16. Similar splitting diagrams can be deduced for a tetrahedral crystal field, providing the splitting is reversed, and the g subscripts are deleted.

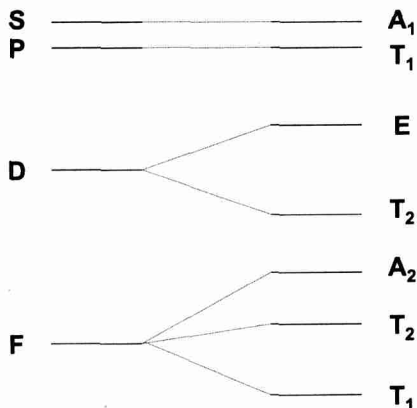


Figure IV.15. The splitting of the ground terms for an octahedral coordination around the TMI (The splitting of the D and F terms under the action of a particular cubic field is not always as depicted here as it may be inverted).

For a d^1 ion (e.g., Ti^{3+}) in an octahedral crystal field, the ground configuration is t_{2g}^1 and the spin multiplicity $S = 2$. The single electron can occupy any of the three degenerate t_{2g} orbitals (orbital degeneracy = 3) and thus the ground state becomes ${}^2T_{2g}$. Absorption of light may result in an excitation of this electron to an e_g orbital and the orbital degeneracy is now equal to 2. As a consequence, the excited e_g^1 state corresponds to a 2E_g term. Conversely, a d^9 ion (e.g., Cu^{2+}) in an octahedral field has the ground configuration $t_{2g}^6e_g^3$ and can be treated as a positive hole. This positive hole can occupy one of the two degenerate e_g orbitals. This is an orbital degeneracy of 2, corresponding to a 2E term. Similarly, the excited $t_{2g}^5e_g^4$ configuration corresponds to a 2T_2 term and the ground term of d^9 is inverted with respect to that of d^1 . The d^1 and d^9 configurations are thus very similar and the same is true for the other d^n pairs: d^2-d^8 , d^3-d^7 and d^4-d^6 (Figure IV.16), but here the situation becomes more complex. We will illustrate this now by taking the d^2 configuration (e.g., V^{3+}) as an example. Exactly the same analysis can be done for the other d^n configurations. The ground configuration t_{2g}^2 of the d^2 configuration permits three degenerate arrangements, which corresponds to a T ground term. If one electron is now excited it will be able to occupy either of the e_g orbitals, while the unexcited electron will be able to occupy any of the three t_{2g} orbitals. This indicates an orbital multiplicity of $2 \times 3 = 5$, which corresponds with two T terms. With the T ground term already described, this makes three T terms with a total orbital multiplicity of 9. Because we started with a 3F ground term ($L = 3$ and $S = 2$) which has an orbital multiplicity of only 7, it implies that the 3F ground term is accompanied by an excited 3P term ($L = 1$ and $S = 2$). This makes in total an orbital multiplicity of 10 ($7 + 3$) of which 9 have so far been explained. The remaining term is a non-degenerate ${}^3A_{2g}$ term and corresponds to the excitation of both electrons to the excited e_g orbitals. This arrangement of electrons is possible because they remain unpaired in these e_g

orbitals. Figure IV.17 shows the electronic configurations of the ground state and the excited states of the d^2 configuration in an octahedral crystal field.

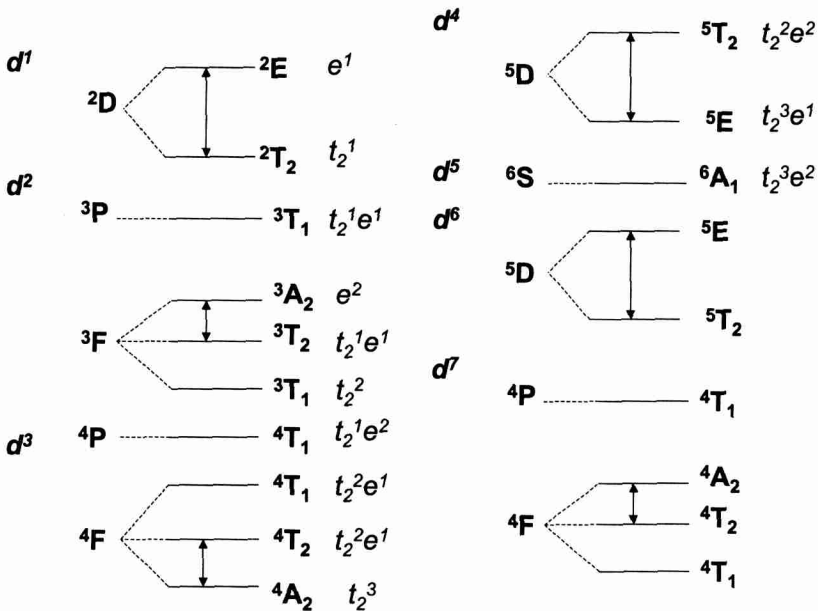


Figure IV.16. Correlation of the spectroscopic ground terms with the electron configuration for d^n ions in an octahedral crystal field.

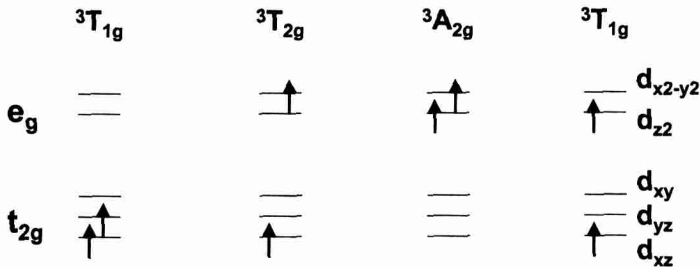


Figure IV.17. Electronic configurations of the ground state and the excited states of the d^2 configuration in an octahedral crystal field.

However, the situation is much more complex as depicted in Figure IV.16 and other spectroscopic terms may arise from each $3d^n$ configuration. A summary of all the spectroscopic terms corresponding to a specific $3d^n$ configuration is summarized in Table IV.2, together with some particular oxidation states of TMI.

Table IV.2. Spectroscopic terms arising from each $3d^n$ configuration for specific oxidation states of TMI (The ground term for each electronic configuration is listed first).

Electronic configuration	TMI	Spectroscopic terms
$3d^0$	Cr^{6+} , V^{5+} , Mn^{7+}	^1S
$3d^1$	Cr^{5+} , V^{4+} , Ti^{3+}	^2D
$3d^2$	V^{3+}	^3F , ^3P , ^1G , ^1D , ^1S
$3d^3$	Cr^{3+} , Mn^{4+}	^4F , ^4P , ^2H , ^2G , ^2F , ^2D , ^2D
$3d^4$	Cr^{2+} , Mn^{3+}	^5D , ^3H , ^3G , ^3F , ^3F , ^3D , ^3P , ^3P , ^1I , ^1G , ^1G , ^1F , ^1D , ^1D , ^1S , ^1S
$3d^5$	Mn^{5+} , Fe^{3+}	^6S , ^4G , ^4F , ^4D , ^4P , ^4P , ^2I , ^2H , ^2G , ^2G , ^2F , ^2F , ^2D , ^2D , ^2P , ^2S
$3d^6$	Fe^{2+} , Co^{3+}	^5D , ^3H , ^3G , ^3F , ^3F , ^3D , ^3P , ^3P , ^1I , ^1G , ^1G , ^1F , ^1D , ^1D , ^1S , ^1S
$3d^7$	Co^{2+}	^4F , ^4P , ^2H , ^2G , ^2F , ^2D , ^2D
$3d^8$	Ni^{2+}	^3F , ^3P , ^1G , ^1D , ^1S
$3d^9$	Cu^{2+}	^2D
$3d^{10}$	Cu^+ , Zn^{2+}	^1S

4.2.1.3. Selection rules and intensity of absorption bands

The intensities of d-d transitions are governed by probabilities of electronic transitions between the different 3d energy levels. The probabilities are expressed by the following two selection rules:

- (1) The spin selection rule: only those transitions are allowed between states of the same spin ($\Delta S = 0$). In other words, only those transitions are allowed which results in a conservation of the number of unpaired electrons in the d orbitals. It is then clear from Figure IV.16 that (a) d^1 , d^4 , d^6 and d^9 ions should produce one spin-allowed d-d transition; (b) d^2 , d^3 , d^7 and d^8 ions should give rise to three spin-allowed transitions; and (c) a d^5 configuration has no spin-allowed d-d transition. The same is true for tetrahedral complexes. Spin-orbital coupling may result into an additional splitting of allowed absorptions and to the appearance of new d-d transitions ($\Delta S = \pm 1$). The spin selection rule can be easily explained for the d^5 configuration: The electronic configuration of these TMI in their ground state is $(t_{2g})^3(e_g)^2$, and all possible excited states have electronic configurations containing fewer unpaired electrons (Figure IV.18). Such transitions are spin-forbidden and have, as a consequence, a very low probability.
- (2) The orbital selection rule: transitions involving only a redistribution of electrons within the same set of atomic orbitals are forbidden or orbitally allowed transitions obey $\Delta l = \pm 1$ with l , the orbital angular momentum quantum number.

This rule is also known as the Laporte or symmetry selection rule. In the latter case, it can be phrased as “in a centrosymmetric molecule only those transitions for which the transition moment integral is different from zero are allowed”. The transition moment integral is $\langle \psi_g | \Delta\mu | \psi_e \rangle$, where ψ_g is the wavefunction of the ground state and ψ_e , the wavelength of the excited state, and $\Delta\mu$ is the operator of the dipole moment change. Group theory is very useful here to evaluate if the integral is different from zero. This is if the direct product of the irreducible representations of ψ_g , $\Delta\mu$ and ψ_e contains the totally symmetric representation of the point group of a TMI complex. Thus a simple inspection of the character tables is sufficient to decide about the allowed d-d transitions. In the case of an octahedral complex, which is centrosymmetric the ground state and excited state are represented by even functions. $\Delta\mu$ transforms as the x, y and z coordinates, which are uneven functions. The product of two even and one uneven function of the total space is zero, and thus all d-d transitions are symmetry forbidden in octahedral complexes. The Laporte selection rule is weakened, or relaxed, by three factors: (a) in the absence of a centre of symmetry. This is the case for tetrahedral complexes. This difference between tetrahedral and octahedral complexes is the reason why a d-d transition of a tetrahedral complex is at least two orders of magnitude more intense than that of an octahedral complex. If both coordination geometries are simultaneously present on a surface, the tetrahedral bands will dominate the spectrum even if the most abundant species is the octahedral one. A typical example of this is Co^{2+} ; (b) mixing of d and p orbitals and (c) interaction between electronic 3d orbital states with vibrational modes, which is called vibronic coupling.

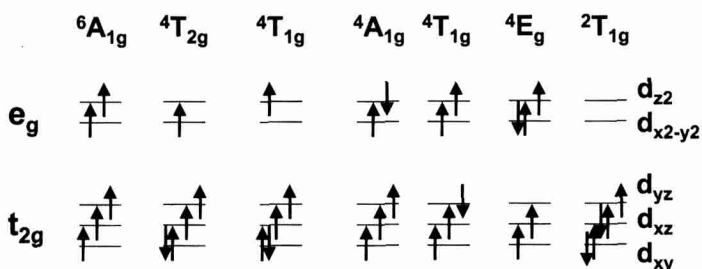


Figure IV.18. Electronic configurations of the ground state and the excited states of the d^5 configuration in an octahedral crystal field.

4.2.2. Ligand field theory

Despite the great success of Crystal field theory in interpreting the d-d transitions of TMI complexes, there is ample evidence that the CF approximation is an oversimplification. This is because the covalency plays an essential part in

coordination chemistry. In order to introduce a degree of covalency, the Racah interelectron repulsion parameter B is introduced. The further the value of B in a coordination complex is reduced below that in the free ion, the more the d-electron charge is assumed to have expanded. This is called the electron cloud expansion or the nephelauxetic effect and ligands can be arranged in a nephelauxetic series, wherein the nephelauxetic effect increases from left to right: $F^- < H_2O < NH_3 < \text{ethylenediamine} < Cl^- < CN^- < Br^- < I^-$. To take account of this effect the electron repulsion is expressed in terms of parameters that are adjustable so as to obtain the best fit between theory and experiment. This is, in fact, the Ligand Field (LF) theory and its corresponding ligand field strength $10Dq$. For octahedral and tetrahedral coordination geometries, explicit ligand field calculations can be found in the literature and the d orbital energy levels can be directly related to the observed d-d transitions.

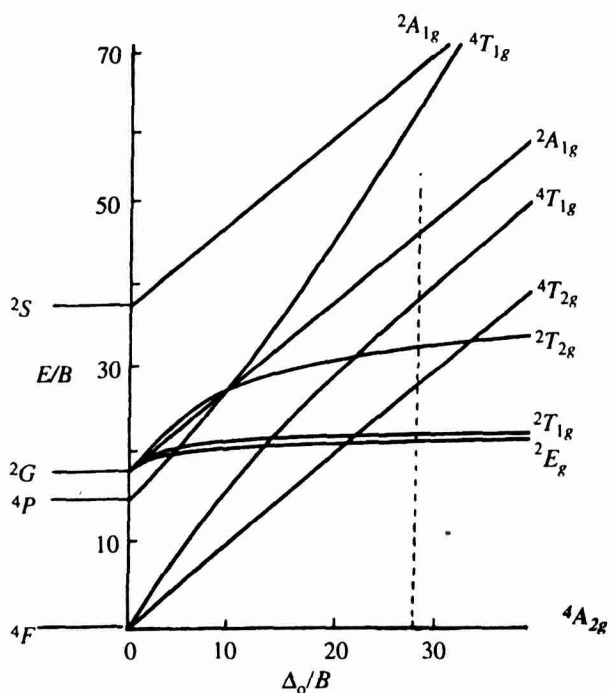


Figure IV.19. The Tanabe-Sugano diagram for the d^3 configuration.

Once the symmetry analysis of a coordination complex of the TMI is done (e.g., O_h , T_d , C_{3v} , etc.) splitting diagrams can be constructed, which allow to carry out quantitative calculations for any strength of ligand field. The most widely used version of such diagram is the so-called Tanabe-Sugano diagram [12], and an example of such a plot is given in Figure IV.19 for a d^3 configuration in an

octahedral coordination. The energies are expressed as E/B and plotted against 10Dq/B. This diagram can now be used for interpreting the spectral data. The two experimentally observed transitions have an energy, which is equal to the two arrows “ ${}^4A_{2g} \rightarrow {}^4T_{2g}(F)$ ” and “ ${}^4A_{2g} \rightarrow {}^4T_{1g}(F)$ ” at a certain 10Dq/B value (Figure IV.19). Hence, one can read the values of 10Dq and B from the location of this point without performing theoretical calculations.

Table IV.3. Racah B parameters for field-free Cr^{n+} and Co^{n+} with $n = 2$ or 3 .

Transition metal ion	Racah B parameter
Cr^{3+}	918
Cr^{2+}	830
Co^{3+}	1100
Co^{2+}	971

Some free-ion values of the Racah B parameter are summarized in Table IV.3. It is clear that the values of B increase with increasing oxidation state. As was stated before, the Racah B parameters are decreased relative to the free-ion values in coordination complexes. For Cr^{3+} in an octahedral coordination, the Racah B parameter is calculated from:

$$B = \frac{1}{3} \left[\frac{(2\nu_1 - \nu_2)(\nu_2 - \nu_1)}{(9\nu_1 - 5\nu_2)} \right] \quad (Eq. IV.11)$$

where ν_1 and ν_2 are obtained from the two spin-allowed transitions ${}^4A_{2g} \rightarrow {}^4T_{2g}(F)$ and ${}^4A_{2g} \rightarrow {}^4T_{1g}(F)$, respectively (Figure IV.16). Some Racah B parameters and ligand field strength values ($\nu_1 = 10Dq$) for different Cr^{3+} -bearing oxides are summarized in Table IV.4. A decreasing B value indicates a lowering of the formal charge on chromium as a result of covalent bonding. This is also expressed by the ratio $\beta = B/B_0$, which is a measure of the nephelauxetic effect or covalent character of the TMI-ligand bonding.

Table IV.4. Racah B parameters and 10Dq values for different Cr^{3+} -bearing oxides with Cr^{3+} in an octahedral ligand field.

Compound	10Dq (cm^{-1})	B
$\alpha-Al_2O_3 (Cr^{3+})$	18000	643
$\alpha-Cr_2O_3 (Cr^{3+})$	16650	624
Cr_2O_3	16600	468
$MgAl_2O_4 (Cr^{3+})$	18000	670
$YCrO_3$	16450	542
$LiCrO_2$	17300	615

4.2.3. Molecular orbital theory

The most complete theory for interpreting absorption spectra is the molecular orbital (MO) theory because it encompasses all possibilities ranging from pure electrostatic to covalent-like bonding. Unfortunately, it is also the most complicated, and quantitative calculations requires the use of modern computing techniques. The fundamental assumption of this theory is that metal and ligand orbitals will overlap and combine to form molecular orbitals, providing they are of the correct symmetries. In one approximation, atomic orbitals of the transition metal ion and atomic or molecular orbitals of the ligands are used to build up the molecular orbitals by the linear combination of the atomic orbital (LCAO) method. This is illustrated in Figure IV.20 for an octahedral complex containing ligands with only σ -bonding and a TMI with d^3 configuration (e.g., Cr^{3+}). There are 6 bonding σ and 6 anti-bonding σ orbitals, together with 3 non-bonding orbitals. The 6 bonding orbitals have more of the character of the ligand orbitals than of the TMI orbitals, while the reverse is true for the anti-bonding molecular orbitals. Thus, the t_{2g} and antibonding e_g orbitals are predominately of TMI 3d orbital character, and the energy separation between these two sets of orbitals is equal to $10Dq$. In CF theory, $10Dq$ was interpreted as the difference in repulsion energy between electrons in pure orbitals of the t_{2g} and e_g groups located at the TMI by the negative charges of the surrounding ligands. Here, $10Dq$ depends on the strength of the metal-ligand bonds and sharing of electrons takes place between ligand orbitals and the TMI 3d orbitals.

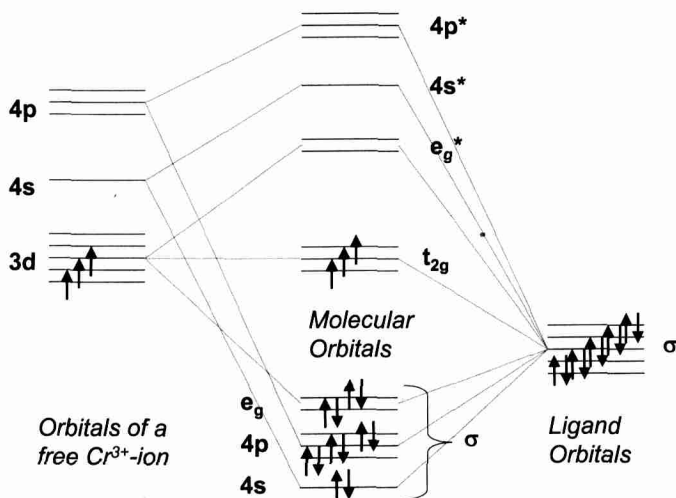


Figure IV.20. Qualitative molecular orbital energy level diagram for the Cr^{3+} ion in octahedral coordination. The diagram refers to σ -bond formation only.

The consequence of the existence of MOs is the occurrence of charge transfer (CT) transitions. They are due to the transition of an electron from a MO with mainly ligand character to a MO with mainly TMI d character. If the ligands have empty low-energy antibonding orbitals (CO, unsaturated organic molecules), a CT transition from a MO with mainly TMI d character to a MO with mainly ligand character is possible. The former is called ligand-to-metal charge transfer (LMCT) transition, whereas the latter is a metal-to-ligand charge transfer (MLCT) transition. In the charge transfer the ligand is formally oxidized and the TMI is reduced (or vice versa). The ease of an electron transfer shows up in the position of the CT band and depends on the electronegativity of the TMI and the ligand.

Tetraoxoanions of TMI with high oxidation numbers provide the most familiar examples of LMCT transitions, and are responsible for their colour. Here, the oxygen lone pair electron is promoted into a lowlying empty e or t_2 TMI orbital. High oxidation states correspond to a low d-orbital population (d^0) and therefore the acceptor level is available and low in energy. This is illustrated for the CrO_4^{2-} anion in Figure IV.21. There are two intense CT bands around 27000 and 37000 cm^{-1} , which are assigned to a $1t_1 \rightarrow 2e$ and $1t_1 \rightarrow 7t_2$ transition, respectively. The other $1t_1 \rightarrow 2e$ transition is (partially) allowed in polyanions of Cr^{6+} , while the $6t_2 \rightarrow 2e$ transition will occur at around 34000 cm^{-1} . Similar CT transitions can be observed for MnO_4^- , ReO_4^- , MoO_4^{2-} , WO_4^{2-} and VO_4^{3-} . Usually, these CT transitions are much more intense and less resolved than d-d transitions. This makes it difficult to assign CT bands to specific transitions and to use them for diagnostic purposes, such as discriminating between different coordination environments (T_d versus O_h) and polymerization degrees (CrO_4^{2-} versus $\text{Cr}_2\text{O}_7^{2-}$ versus $\text{Cr}_3\text{O}_{10}^{6-}$). As a rule of thumb, one can say that: (1) a CT for a tetrahedral complex is located at higher energy than that of an octahedral complex and (2) the more polymerized a tetraoxoanion of a TMI, the lower in energy its CT transitions will occur.

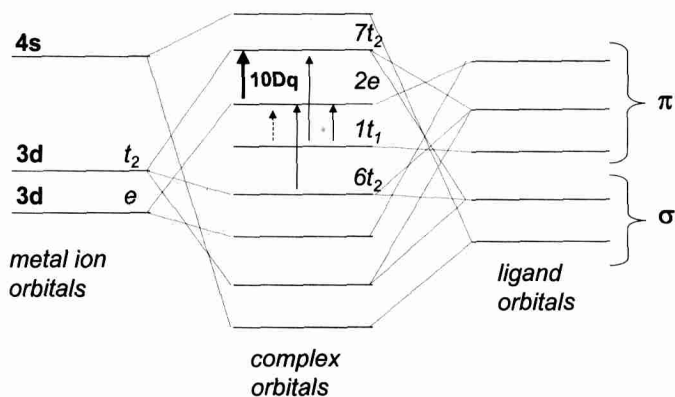


Figure IV.21. Energy diagram of the CrO_4^{2-} anion and the corresponding charge transfer transitions of type $O \rightarrow \text{Cr}^{6+} (d^0)$.

4.3. Selected examples

In the next section we will discuss, the strength and weakness of DRS spectroscopy for obtaining detailed information about the distribution of coordination geometries and oxidation states of TMI on surfaces. We will limit ourselves to a detailed discussion of Cr, V, Co and Cu because these elements have been studied in great detail in our laboratory. Five subjects will be treated:

- (1) Discriminating between and quantifying of different oxidation states of TMI on surfaces;
- (2) Development of structure-activity relationships based on *in situ* DRS spectroscopy;
- (3) Discriminating between framework and extra-framework TMI in molecular sieves;
- (4) Discriminating between different complexes of a TMI on the surface of zeolites and clay minerals;
- (5) Coordination of TMI in zeolites

4.3.1. Discriminating between and quantifying of different oxidation states of TMI on surfaces

Chromium will be taken as an example because it occurs with different coordination numbers (2, 3, 4, 5 and 6), different oxidation states (Cr^{n+} with $n = 2, 3, 4, 5$ and 6) and molecular structures (chromate, dichromate, trichromate, etc.) on inorganic surfaces. This chameleon-type behavior makes the analysis of this element rather involved, and its study requires a multi-technique approach. This approach has to be partially based on DRS because this technique is sensitive to the oxidation state and coordination environment of Cr^{2+} , Cr^{3+} and Cr^{6+} .

4.3.1.1. Discriminating between oxidation states of Cr

Figure IV.22 shows a set of deconvoluted DRS spectra of a reduced 0.2 wt% Cr/ Al_2O_3 catalyst as a function of the reduction temperature. All the deconvoluted spectra have a broad and intense shoulder starting at 40000 cm^{-1} and increasing in intensity up to 50000 cm^{-1} . This band is due to the alumina support. Because the DRS spectrum of the alumina support was already subtracted from the DRS spectra of the Cr-catalyst, it suggests that the support in the presence of Cr is different from the parent support. Thus, there is a strong Cr-support interaction.

Spectrum A in Figure IV.22 is characterized by two intense bands at 27000 and 41400 cm^{-1} . By deconvolution of the spectrum two low frequency shoulders at 22500 and 34400 cm^{-1} are resolved. All these bands are charge-transfer transitions and the deconvoluted spectrum is typical for chromate [13]. The assignments of the four transitions are given in Figure IV.21. The reduction of Cr on alumina starts above 200°C and is accompanied with typical color changes. The chromate bands gradually decrease in intensity with increasing reduction temperature at the expense of weak low frequency d-d absorption bands due to Cr^{3+} and Cr^{2+} . The exact band positions of

dehydrated Cr^{6+} , Cr^{2+} and Cr^{3+} on alumina, obtained by deconvolution of the spectra, are summarized in Table IV.5. According to Figure IV.16, these d-d transitions can be assigned in the following way: (a) Cr^{3+} in pseudo-octahedral coordination: 17000 cm^{-1} (${}^4\text{A}_{2g} \rightarrow {}^4\text{T}_{2g}$); 23000 cm^{-1} (${}^4\text{A}_{2g} \rightarrow {}^4\text{T}_{1g}$ (F)) and 33000 cm^{-1} (${}^4\text{A}_{2g} \rightarrow {}^4\text{T}_{1g}$ (P)); and (b) Cr^{2+} in pseudo-tetrahedral coordination: 12500 cm^{-1} (${}^5\text{E}_g \rightarrow {}^5\text{T}_{2g}$).

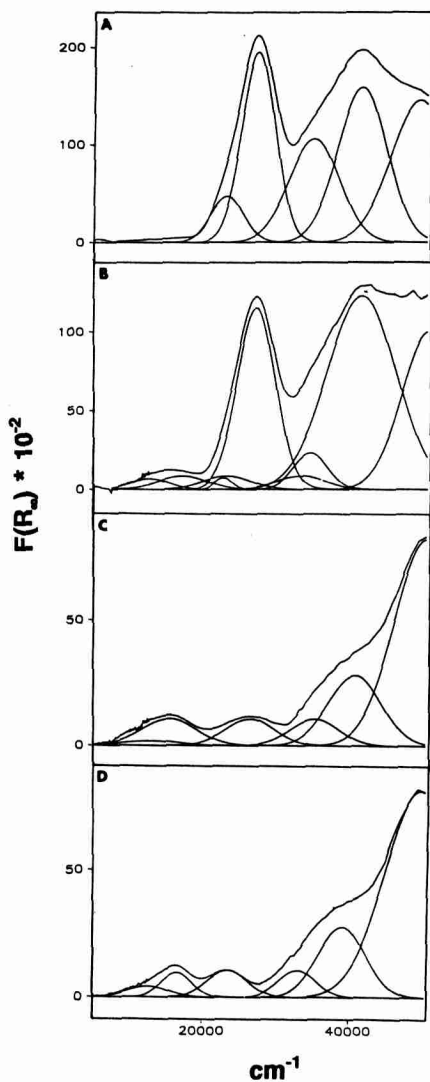


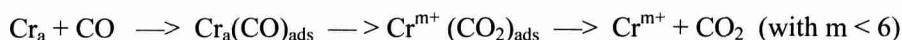
Figure IV.22. Deconvoluted DRS spectra of reduced 0.2 wt% $\text{Cr}/\text{Al}_2\text{O}_3$; the reduction temperature is equal to (A) 200°C ; (B) 300°C ; (C) 400°C ; and (D) 600°C . The reducing agent is CO (American Chemical Society, Copyright 1993).

reduction with CO for Cr/SiO₂ and Cr/Al₂O₃ catalysts, whereas Cr/SiO₂.Al₂O₃ catalysts have an intermediate average oxidation state.

Table IV.6. Cr²⁺:Cr³⁺ ratios on 0.1 wt% Cr on different supports by DRS.

Cr-catalyst	Cr ²⁺ :Cr ³⁺ ratio after reduction at		
	300°C	400°C	600°C
Cr/silica	0.2	0.1	0.1
Cr/silica-alumina	1.3	1.3	2.9
Cr/alumina	0.9	1.1	0.8

Another interesting approach is to use the intensity of the 27000 cm⁻¹ Cr⁶⁺ band during a CO reduction process in the *in situ* DRS cell (Figures IV.7 and IV.8) in order to derive information about the reduction kinetics [16]. It was found that the intensity of the 27000 cm⁻¹ Cr⁶⁺ band follows a two-exponentials decay both for Cr/SiO₂ and Cr/Al₂O₃, but the decay is much faster for SiO₂ than for Al₂O₃. The following reaction scheme can explain the data:



The rate determining step is the reduction of Cr⁶⁺ by CO with formation of carboxylates, which decompose to CO₂. The rate constant, k₂, tabulated in Table IV.7, is 1 to 2 order larger for Cr/SiO₂ than for Cr/Al₂O₃. This may have to do with differences in dispersion, a much stronger interaction of Cr⁶⁺ with alumina than with silica; and a better stabilization of the Cr³⁺ and Cr⁵⁺ oxidation states on alumina.

Table IV.7. Calculated rate constant k₂ for 0.5 wt% Cr/SiO₂ and 0.4 wt% Cr/Al₂O₃ catalysts at different reaction temperatures in the reduction with CO as obtained from *in situ* DRS spectroscopy.

Temperature (°C)	Calculated rate constant k ₂ (min ⁻¹) x 10 ⁵	
	0.5 wt% Cr/SiO ₂	0.4 wt% Cr/Al ₂ O ₃
400	43.2	2.4
500	1105.9	47.7

It is important to notice that the above described quantitative approach has been extended to supported vanadium oxide catalysts [17] and Cr-loaded zeolites [18]. In the latter case, useful information about the redox behavior of Cr⁶⁺ in zeolites could be revealed by monitoring the relative intensity of the 27,000 cm⁻¹ CT band of Cr⁶⁺ as a function of the reduction temperature in the presence of CO. This is illustrated in Figure IV.26. This figure shows that:

- (a) CO reduction starts above 200°C, except for Cr-Mordenite;
 (b) the amount of Cr⁶⁺ is zero after reduction at 600°C, except for a Cr-Y zeolite prepared *via* the solid state ion exchange procedure; and
 (c) the relative decrease of Cr⁶⁺ in the region 200-600°C, when used as a reducibility criterion, follows the sequence: Cr-Y (solid state) < Cr-GaY < Cr-X < Cr-Y (ion exchange) < Cr-Y (impregnation) < Cr-Mordenite; and
 (d) after recalcination, all the Cr⁶⁺ is reestablished.
 These differences in redox behavior of Cr could be explained in terms of zeolite properties and Cr dispersion [18].

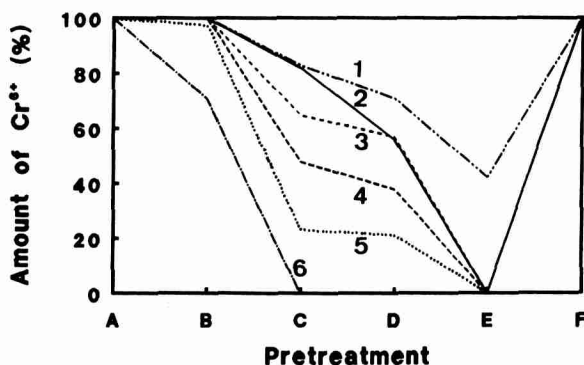


Figure IV.26. Amount of Cr⁶⁺ as a function of different pretreatments: (A) calcination at 550°C; (B) reduction at 200°C; (C) reduction at 300°C; (D) reduction at 400°C; (E) reduction at 600°C; (F) recalcination at 550°C; and zeolites: (1) Cr-Y prepared via the solid state ion exchange procedure; (2) Cr-GaY; (3) Cr-NaX; (4) Cr-Y prepared via ion exchange; (5) Cr-Y prepared via impregnation and (6) Cr-Mordenite (Butterworth-Heinemann, Copyright 1994).

4.3.1.3. Discriminating between molecular structures of Cr

Figure IV.22 clearly illustrates the difficulties mostly encountered in the analysis of DRS spectra of supported metal oxide catalysts; *i.e.*, experimental DRS spectra are a combination of spectra of individual oxidation states and/or coordination environments of a TMI, in this case tetrahedral Cr⁶⁺, pseudo-octahedral Cr³⁺ and pseudo-octahedral Cr²⁺. This makes spectral analysis difficult, and unbiased information can only be obtained by applying chemometrical techniques, such as principal component analysis (PCA), factor analysis (FA) and partial least squares (PLS). Details about these techniques can be found in several textbooks and research papers [19-22]. The general scheme is as follows: The data matrix D, consisting of n spectra, each with m datapoints, is decomposed as a linear combination of spectra of independent pure components, each with a specific weight. These weights are proportional to the concentrations of the pure components in the mixtures in

accordance with the equivalent of Beer's law, namely the Kubelka-Munk function (Eq. IV.3).

An interesting chemometrical technique for spectral analysis is SIMPLISMA (simple-to-use-interactive-self-modeling-analysis) developed by Windig [23-25], because it gives not only the number of pure components and their spectra, but the researcher can also intervene and decide by himself whether to accept a pure component or not. An example of the application of the *SIMPLISMA* technique is given in Fig. IV.27 for DRS spectra of hydrated $\text{Cr}/\text{SiO}_2\cdot\text{Al}_2\text{O}_3$ catalysts as a function of the $\text{SiO}_2:\text{Al}_2\text{O}_3$ ratio [26]. Four pure spectra are revealed in the DRS spectra of supported Cr catalysts, which are shown in Fig. IV.28: Component A with three characteristic bands at 493 nm (20300 cm^{-1}), 327 nm (30600 cm^{-1}) and 227 nm (44100 cm^{-1}); component B with three bands at 402 nm (24900 cm^{-1}), 273 nm (36600 cm^{-1}) and 220 nm (45500 cm^{-1}); component C appeared at 565 nm (17700 cm^{-1}); and component D absorbs in the region 350-270-204 nm ($28600\text{-}37000\text{-}49000\text{ cm}^{-1}$). Components A and B are due to chromate and dichromate, respectively, and their relative ratio increases with decreasing $\text{SiO}_2:\text{Al}_2\text{O}_3$ ratio. Component C is assigned to pseudo-octahedral Cr^{3+} , while component D is a support band. The same analysis can be successfully applied on calcined and reduced supported Cr catalysts [25]. Thus, the *SIMPLISMA* technique is a viable alternative to the earlier developed *Grams/386* method, and we propose this method as an interesting tool for investigating complex spectra of supported metal oxide catalysts.

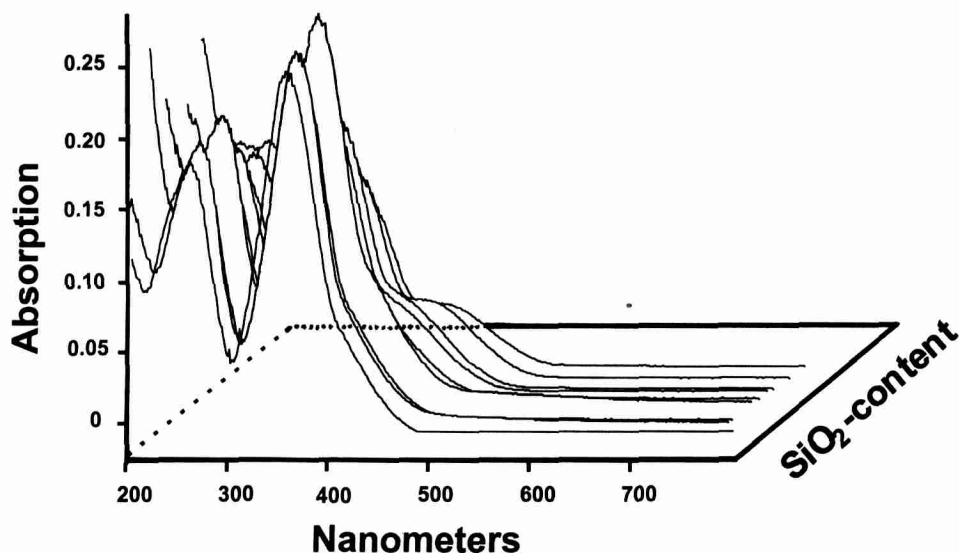


Figure IV.27. DRS spectra of 0.2 wt% $\text{Cr}/\text{SiO}_2\cdot\text{Al}_2\text{O}_3$ catalysts as a function of the $\text{SiO}_2:\text{Al}_2\text{O}_3$ ratio (Academic Press, Copyright 1997) : the front curve with no shoulder at 450 nm is that for a pure Al_2O_3 support, whereas the curve with the most pronounced shoulder at 450 nm is that for a pure SiO_2 support.

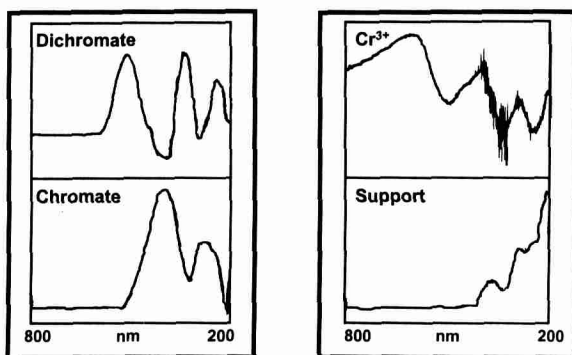


Figure IV.28. Pure component spectra of the DRS spectra of Figure IV.26 (Academic Press Copyright 1997).

4.3.2. Development of structure-activity relationships based on *in situ* DRS spectroscopy

The *in situ* DRS cell of Figures IV.7 and IV.8, in combination with *on line* gas chromatography (GC) analysis, can be used for the development of quantitative structure-activity relationships in the field of heterogeneous catalysis. This will be illustrated for the industrially important dehydrogenation of isobutane over supported chromium oxide catalysts [27].

This recently developed method involves a four-pronged approach [28]. In a first step, the number of required experiments was optimized by using an experimental design. Five factors were selected to describe the dehydrogenation process; *i.e.*, SiO₂:Al₂O₃ ratio of the support, expressed as the isoelectric point (IEP) (X₁), Cr loading (X₂), gas composition (X₃), reaction temperature (X₄) and reaction time (X₅), and a 5-level circumscribed central composite experimental design, generated by *MODDE for Windows* (Umetri AB), resulted in a set of 30 experiments.

Secondly, the dehydrogenation activity was measured by *on line* GC analysis, respectively. This operation allowed to develop a quantitative relationship between the different factors and the dehydrogenation activity, expressed as $y^{1/2}$:

$$y^{1/2} (\%) = 2.284 - 0.195X_1 + 0.121X_2 - 0.132X_3 - 9.540 \cdot 10^{-4}X_4 - 0.0610X_5 + 4.941 \cdot 10^{-3}X_3^2 + 5.875 \cdot 10^{-4}X_5^2 + 5.137 \cdot 10^{-4} \cdot X_1 \cdot X_4 - 4.480 \cdot 10^{-3}X_2 \cdot X_3 + 8.008 \cdot 10^{-4}X_3 \cdot X_5$$

(Eq. IV.12)

Eq. IV.12 allows to calculate the conditions for maximum dehydrogenation activity over supported chromium oxide catalysts. The following conditions were obtained: X₁ = 8; X₂ = 7.5; X₃ = 2; X₄ = 500 and X₅ = 10. Thus, a maximum conversion is obtained after 10 minutes for a 7.5 wt% Cr/Al₂O₃ catalyst at 500°C with a mixture of 2% isobutane in N₂. In order to visualize Eq. IV.12, one can make conversion surface plots, as illustrated in Figure IV.29.

For example, Figure IV.29A predicts the catalytic activity after 30 minutes for a Cr/SiO₂.Al₂O₃ catalyst at 425°C as a function of the amount of isobutane in N₂ and as a function of the Cr loading. It is clear that the dehydrogenation activity gradually increases with increasing Cr loading and decreasing amount of isobutane in N₂.

The influence of the reaction time and the Cr loading on the predicted dehydrogenation activity of a Cr/SiO₂.Al₂O₃ catalyst at 425°C is illustrated in Figure IV.29B. It shows a gradual decrease in activity with increasing reaction time. The combined effect of the IEP of the support of the support and the reaction temperature on the catalytic activity is given in Figure IV.29C. One can notice that at high reaction temperatures the dehydrogenation activity increases with increasing IEP; *i.e.*, with an increasing amount of Al₂O₃ in the support.

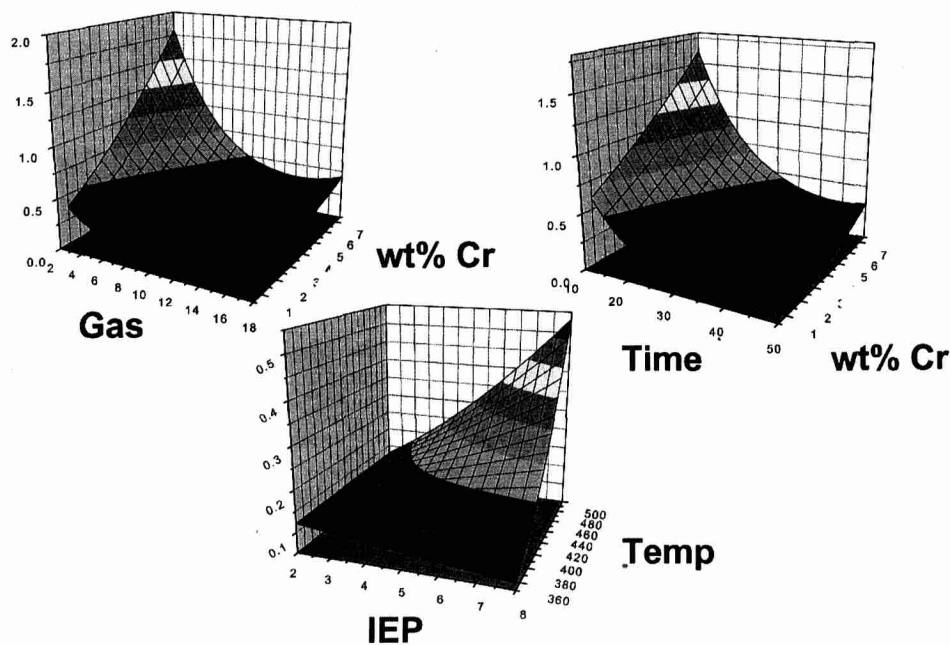


Figure IV.29: (A) Conversion surface plot of the gas composition and Cr-loading (The reaction temperature, isoelectric point of the support and the reaction time are 425°C, 5 and 10 minutes, respectively); (B) Conversion surface plot of the reaction time and Cr loading (The isoelectric point, gas composition and reaction temperature are 5, 10% isobutane and 425°C, respectively); and (C) Conversion surface plot of the isoelectric point of the support and the reaction temperature (The Cr loading, gas composition and reaction time are 4 wt%, 10% isobutane and 30 minutes, respectively) (Elsevier Science B.V., Copyright 2000).

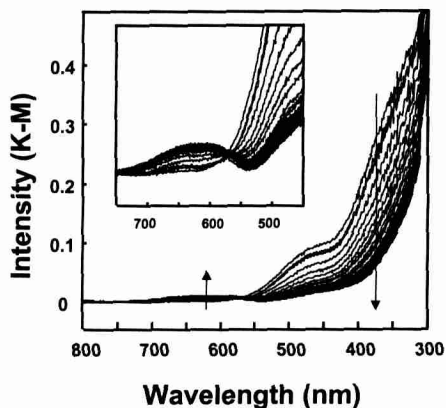


Figure IV.30 In situ DRS spectra of 0.5 wt% Cr/SiO₂ catalyst treated at 350°C in 2% isobutane in N₂ as a function of time (Elsevier Science B.V., Copyright 2000).

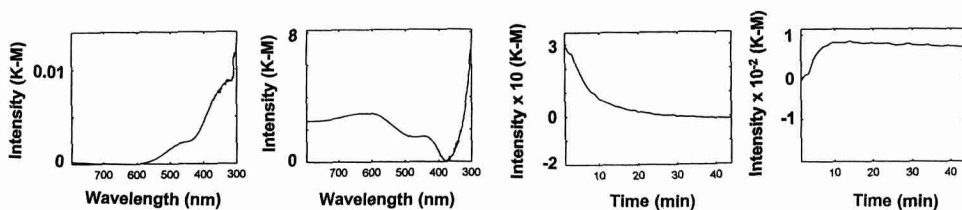


Figure IV.31. Pure component spectra of the in situ DRS spectra of Figure IV.30 (Elsevier Science B.V., Copyright 2000).

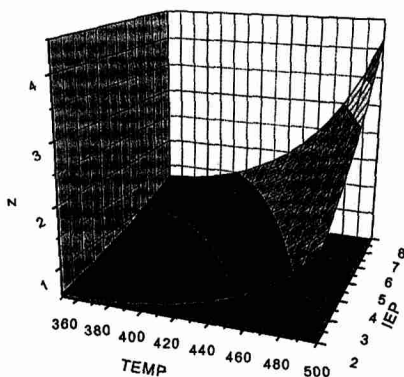


Figure IV.32. Reduced chromium surface plot of the reaction temperature and the isoelectric point of the support (The chromium loading is 7.5 wt%) (Elsevier Science B.V., Copyright 2000).

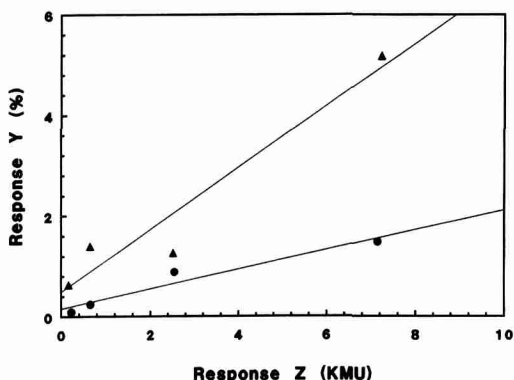


Figure IV.33. Quantitative relationship between the catalytic activity (response Y) and the amount of reduced Cr (response Z) as predicted for 10 (▲) and 50 (●) minutes on stream (Elsevier Science B.V., Copyright 2000).

Thirdly, the Cr-speciation was measured by *in situ* UV-VIS DRS spectroscopy. An example of a set of *in situ* DRS spectra is given in Figure IV.30. This is an experiment with a 0.5 wt% Cr/SiO₂ catalyst treated at 350°C in 2% isobutane. Figure IV.30 shows a gradual decrease of absorption maxima around 360 (27700 cm⁻¹) and 450 nm (22200 cm⁻¹) with increasing reaction time at the expense of a new weak band with an absorption maximum at around 625 nm (16000 cm⁻¹). The insert of Figure IV.30 illustrates the presence of an isobestic point, suggesting the presence of two different Cr-species. By applying the *SIMPLISMA* technique to the set of DRS spectra of Figure IV.31, two pure component spectra were obtained. The two pure component spectra have absorption maxima around 360 (27700 cm⁻¹) and 625 nm (16000 cm⁻¹). The first pure component spectrum is typical for Cr⁶⁺, whereas the second pure component spectrum is indicative for the presence of Cr^{2+/3+}. Figure IV.32 illustrates the effect of the reaction temperature and the support composition on the K-M(Cr^{2+/3+}) (z) values. It is clear that the band intensity increases with increasing reaction temperature and IEP of the support.

In a final step, a mathematical relation, which relates the dehydrogenation activity with the amount of *in situ* measured Cr^{3+/2+} was derived. This is illustrated in Figure IV.33 for Cr/Al₂O₃ catalysts. It can be concluded that the catalytic activity (response Y) is directly proportional with the amount of reduced Cr (response Z). The difference in catalytic activity between Cr/Al₂O₃ catalysts, which were 10 or 50 minutes on stream, must be explained in terms of coking. Finally, it is important to stress that the present analysis does not discriminate between Cr²⁺ and Cr³⁺, and thus, does not allow to unambiguously assign the catalytic activity to one of these species. In any case, we have indications that Cr²⁺ is less active than Cr³⁺ for alkane dehydrogenation. Thus, only *in situ* DRS spectroscopy is not sufficient to resolve this issue, and other techniques such as *in situ* ESR spectroscopy have to be called in.

4.3.3. Discriminating between framework and extra-framework TMI in molecular sieves

In the last two decades many research groups in the field of molecular sieve science have tried to incorporate TMI, such as Co, Cr and V, in the framework of molecular sieves [29,30]. An important group of molecular sieves are the microporous crystalline aluminophosphates ($\text{AlPO}_4\text{-}n$) where Al and/or P can – in principle – be replaced by a TMI. This substitution reaction is often coined as isomorphous substitution. Although many TMI are claimed to incorporate in the framework of these molecular sieves, only for Co^{2+} has conclusive evidence been presented in the literature. But even in the case of $\text{CoAPO-}n$ molecular sieves, it is not uncommon to observe both framework and extra-framework Co^{2+} -species. DRS spectroscopy has shown to be very useful for discriminating between framework and extra-framework Co^{2+} . The basis for this discriminating power originates from the differences in spectroscopic properties between octahedral and tetrahedral Co^{2+} . Two reasons can be formulated: (a) the position of the absorption maxima will be different for both type of Co^{2+} complexes ($10Dq(\text{O}_h) > 10Dq(\text{T}_d)$); and (b) the intensities of both type of Co^{2+} complexes are different. Indeed, according to the Laporte selection rule (section 4.2.1.3.) the three allowed d-d transitions of an octahedral Co^{2+} complex are much less intense than that of d-d transitions of a tetrahedral Co^{2+} complex.

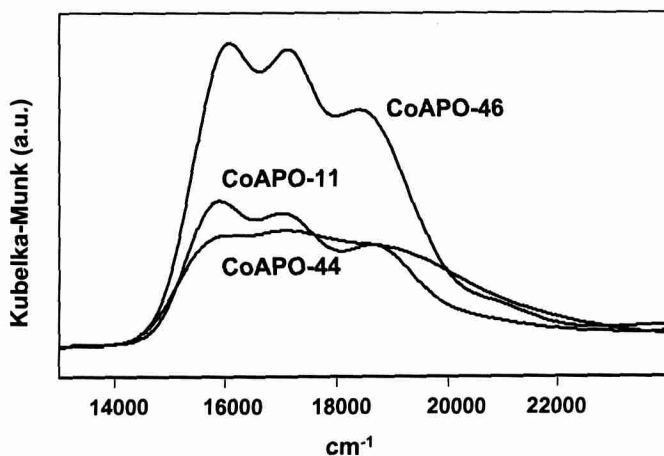


Figure IV.34. DRS spectra of as-synthesized CoAPO-11 , -44 and -46 materials.

An example of a set of DRS spectra of as-synthesized CoAPO-11 , -44 and -46 materials is given in Figure IV.34 [31]. Each of these crystalline materials is characterized by a triplet absorption band at around 17000 cm^{-1} , which can be assigned to the ${}^4\text{A}_2(\text{F}) \rightarrow {}^4\text{T}_1(\text{P})$ transition of tetrahedrally coordinated Co^{2+} . The

weak absorption at around 21000 cm^{-1} is due to the ${}^4\text{T}_{1g}(\text{F}) \rightarrow {}^4\text{T}_{1g}(\text{P})$ transition of octahedrally coordinated Co^{2+} . It is clear that the triplet bands of tetrahedral Co^{2+} dominates the DRS spectra. This is not the case if a less-crystalline, dense or amorphous material is synthesized. This is illustrated in Figure IV.35, where the deconvoluted DRS spectra of a crystalline and an almost amorphous CoAPO-n material are compared with each other. The black area represents the fraction of tetrahedral Co^{2+} in the DRS spectrum, whereas the gray area represents octahedral or extra-framework Co^{2+} located at the surface of the $\text{AlPO}_4\text{-n}$ materials. It is clear that the framework crystallinity is correlated with the $\text{Co}^{2+}_{\text{tetrahedral}}:\text{Co}^{2+}_{\text{octahedral}}$. This is shown in Figure IV.36 for a whole set of CoAPO-n materials differing in their crystallinity [31]. It is then assumed that the fraction of tetrahedral Co^{2+} is incorporated in the lattice of these CoAPO-n molecular sieves.

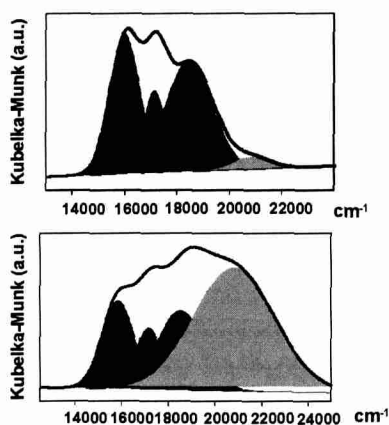


Figure IV.35. Deconvoluted DRS spectra of (A) a well-crystalline as-synthesized CoAPO-46 sample and (B) an almost amorphous as-synthesized CoAPO-11 sample.

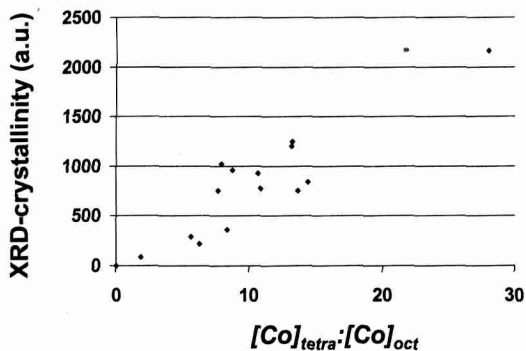


Figure IV.36. Relation between the $\text{Co}^{2+}_{\text{tetrahedral}}:\text{Co}^{2+}_{\text{octahedral}}$ ratio and the overall crystallinity of as-synthesized CoAPO-n materials.

The situation is clearly different for CrAPO-5 molecular sieves and a set of typical DRS spectra of the green colored as-synthesized CrAPO-5 samples with increasing Cr content are shown in Figure IV.37 [32]. The DRS spectra are characterized by two absorption bands at 15900 and 21800 cm^{-1} , and the intensities of both transitions almost linearly increase with increasing Cr content. Based on the Racah B parameters and 10Dq values for different Cr^{3+} -bearing oxides with Cr^{3+} in an octahedral ligand field (Table IV.4), one can evaluate the coordination of Cr^{3+} in the AlPO_4 -5 system. The d-d absorption bands can be assigned to the ${}^4\text{A}_{2g} \rightarrow {}^4\text{T}_{2g}$ and ${}^4\text{A}_{2g} \rightarrow {}^4\text{T}_{1g}(\text{F})$ transitions of octahedral Cr^{3+} , and no indications of tetrahedral Cr^{3+} can be found in the spectra. Indeed, the relatively intense absorption band of tetrahedral Cr^{3+} expected at around 7000 cm^{-1} is not observed. In addition, the 10Dq value and B parameter are equal to 15900 cm^{-1} and 577, which is close to the values reported for Cr_2O_3 . This indicates that Cr is most probably located outside the lattice in cluster-type surroundings on the surface of the AlPO_4 -5 material.

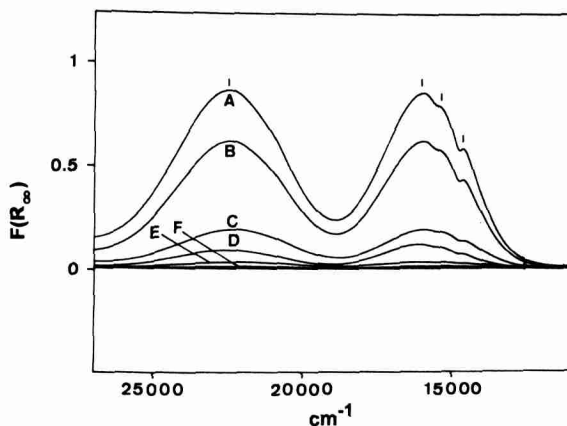


Figure IV.37. DRS spectra of as-synthesized CrAPO-5 materials as a function of the chromium content: $0.75\text{R}(\text{Cr}_x\text{Al}_y\text{P}_z)\text{O}_4 \cdot 20\text{H}_2\text{O}$ with $x =$ (A) 0.08; (B) 0.04; (C) 0.02; (D) 0.004; (E) 0.002 and (F) 0.0 (Butterworth-Heinemann, Copyright 1994).

Similar observations were made for VAPO-5 molecular sieves and V^{4+} is always present as a (pseudo-) octahedral species in this molecular sieve [33].

4.3.4. Discriminating between different complexes of TMI on the surface of zeolites and clay minerals

Another interesting research topic is the immobilization of TMI complexes on the surface of zeolites and clay minerals. Here, DRS can be used to differentiate between transition metal ion complexes having a different composition of the first

coordination sphere. An illustrative example is the ion exchange of $\text{Cu}(\text{histidine})_n^{m+}$ and $\text{Cu}(\text{lysine})_n^{m+}$ complexes onto zeolite Y and saponite clays [34,35, 36]. The coordination complexes of Cu^{2+} typically consist of four nearby donor atoms arranged approximately in a plane around the metal ion with the possibility of one or two more distant axial donors. Amino acids, such as histidine and lysine, can act as tri- or bidentate ligands and can offer N (α -amino, ϵ -amino or imidazole) and O (carboxylate) as donor atoms. As was discussed before – according to the spectrochemical series – N atoms are known to pose a stronger ligand field around Cu^{2+} than O atoms and therefore the d-d transition will shift to higher energy if more N atoms are in the first coordination sphere around Cu^{2+} .

An example of a DRS spectrum of $\text{Cu}(\text{lysine})$ complexes exchanged in zeolite Y is given in Figure IV.38. The DRS spectrum is characterized by two absorption bands at 16200 and 40000 cm^{-1} . The d-d transition at 16200 cm^{-1} is clearly different from the d-d absorption of a $\text{Cu}(\text{H}_2\text{O})_6^{2+}$ complex in zeolite Y (Table IV.8), indicating that N atoms are coordinating to Cu^{2+} . Other evidence for this coordination comes from the ligand to metal charge transfer (LMCT) band at around 40000 cm^{-1} .

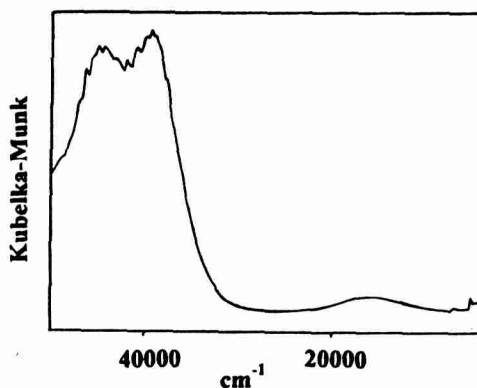


Figure IV.38. DRS spectrum of $\text{Cu}(\text{lysine})$ complexes exchanged in zeolite Y (American Chemical Society, Copyright 1996).

The d-d absorption bands of $\text{Cu}(\text{lysine})$ and $\text{Cu}(\text{histidine})$ complexes in zeolite Y and saponite clays are compared in Table IV.8. This table indicates that the d-d absorption maxima are systematically higher in energy for clays than for zeolites. This indicates that the complexes are more square planar-like on the bidimensional surface of saponite than in the supercages of zeolite Y. This may be due to the removal of: (1) solvent (H_2O) molecules in axial positions; or (2) axially coordinating atoms (carboxylate) of the amino acid. The former is likely to occur for lysine, the latter for the histidine complexes. This difference between both complexes might explain why the effect is more pronounced for histidine molecules. Not much, however, can be said about the in-plane coordinating atoms based on the

DRS absorption bands only and other techniques, such as ESR and pulsed ESR [37], have to be called in. We assume the predominance of bis-complexes with an in-plane coordination as in solution; *i.e.*, NNOO for lysine and NNNO for histidine. Evidence for the latter can be found in the 7-line superhyperfine splitting as observed by X-band ESR. In any case, the complexes have a planar-like – most probably NNOO/NNNO - configuration in both zeolites and clay minerals.

Table IV.8. Survey of the DRS absorption bands of immobilized Cu complexes in zeolite Y and saponite clays.

Material	d-d transition (cm^{-1})
$\text{Cu}(\text{H}_2\text{O})_6^{2+}$ -saponite clay	13100
$\text{Cu}(\text{H}_2\text{O})_6^{2+}$ -zeolite Y	12500
$\text{Cu}(\text{lysine})_2^{2+}$ -saponite clay	16700
$\text{Cu}(\text{lysine})_2^{2+}$ -zeolite Y	16200
$\text{Cu}(\text{histidine})_2^{2+}$ -saponite clay	16700
$\text{Cu}(\text{histidine})_2^{2+}$ -zeolite Y	15600

4.3.5. Coordination of TMI in zeolites

Because zeolites are crystalline materials with crystallographically well-defined coordination sites at their surface, TMI will occupy in these materials after dehydration distinct surface sites. The site symmetries and the coordination distances TMI–surface oxygens are known and a detailed account on this subject has been given by W.J. Mortier [38]. The structure and the different cation sites of zeolite A and zeolites X and Y are given in Figure IV.39.

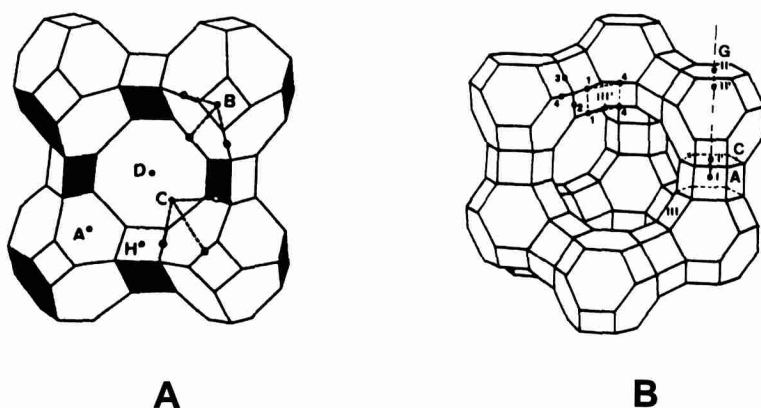


Figure IV.39. Zeolite A (A) and zeolites X and Y (B) - The cation sites (Roman numerals) and crystallographically different oxygen ions (Arabic numerals) are also included.

With this information it is - in principle - possible to give a detailed interpretation of the d-d spectra of TMI located at these coordination sites. Typical DRS spectra of Cu^{2+} and Co^{2+} coordinated to a sixring of oxygens are shown in Figure IV.40 [39]. Originally, these electronic spectra have been interpreted in the frame of a trigonal ligand field of point group C_{3v} or D_{3h} , as provided by the available XRD data [40]. These interpretations are given in Table IV.9.

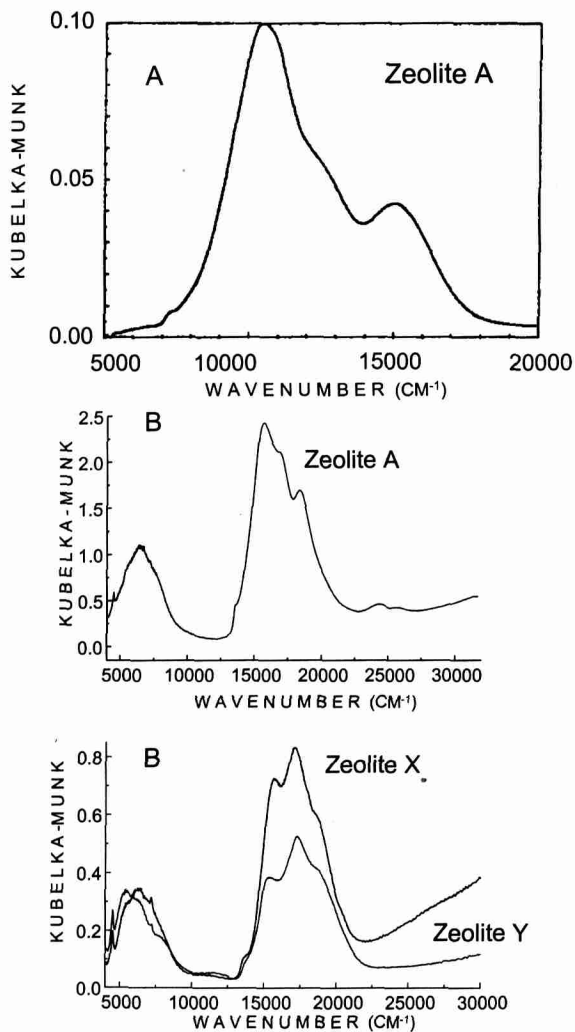


Figure IV.40. Typical DRS spectra of Cu^{2+} (A) and Co^{2+} (B) coordinated to a sixring of oxygens.

Table IV.9 Interpretation of the DRS spectra of Cu^{2+} and Co^{2+} coordinated to a sixring of oxygens based on ligand field calculations [40].

Band maximum (cm^{-1})	Assignment	
Cu^{2+}	D_{2h} (Klier <i>et al.</i>)	C_{3v} (Schoonheydt <i>et al.</i>)
10700	${}^2\text{E}_1 \rightarrow {}^2\text{E}_2$	${}^2\text{E}_1 \rightarrow {}^2\text{A}_1$
12700	${}^2\text{E}_1 \rightarrow {}^2\text{E}_2^+$	${}^2\text{E}_1 \rightarrow {}^2\text{E}_2^-$
14500	${}^2\text{E}_1 \rightarrow {}^2\text{A}_1$	${}^2\text{E}_1 \rightarrow {}^2\text{E}_2^+$
Co^{2+}		
6000-8000	${}^4\text{E}''({}^4\text{F}) \rightarrow {}^4\text{E}'({}^4\text{F})$	${}^4\text{E}''({}^4\text{F}) \rightarrow {}^4\text{E}'({}^4\text{F})$
15000-19000	${}^4\text{E}''({}^4\text{F}) \rightarrow {}^4\text{A}_1'', {}^4\text{A}_2''({}^4\text{F})$	${}^4\text{E}''({}^4\text{F}) \rightarrow {}^4\text{P manifold}$
24000-25000	${}^4\text{E}''({}^4\text{F}) \rightarrow {}^4\text{E}''({}^4\text{P})$	Idem

There are several comments to be made about Table IV.9:

- In the trigonal field, there are three oxygens in the primary coordination sphere. The d-d band positions are found in the range of regular tetrahedral and octahedral complexes. This means that the three oxygens of the framework give a ligand field as strong as that of four to six oxygens in a regular inorganic complex.
- For Cu^{2+} the ground state is doubly degenerate, thus giving rise to Jahn-Teller splitting. The Jahn-Teller radius R , found to be 16.5–20.3 pm [41], expresses the distortion from trigonal symmetry.
- The trigonal d-level splitting proposed by Klier is different from that proposed by Schoonheydt *et al.* [40]. In terms of angular overlap model parameters, Klier's sequence of levels leads to a physically unacceptable π -bonding parameter, at least for oxygen ligands.
- A similar remark can be made about the interpretation of the Co^{2+} spectra. The splitting of the ${}^4\text{F}$ manifold as proposed in Table IV.9 by Klier *et al.* [39,40] also results in an extremely high π character of the Co^{2+} -O bond [41].

To overcome these difficulties a different strategy was developed [41, 42]. The sixring site was modelled with the clusters $\text{TMIO}_6\text{Si}_{6-x}\text{Al}_x(\text{OH})_{12}^{(2-x)+}$ and $\text{TMIO}_6\text{Si}_{6-x}\text{Al}_x\text{H}_{12}^{(2-x)+}$ (with TMI = Co^{2+} or Cu^{2+}). They are shown for Co^{2+} in Figure IV.41. In the ring of these clusters there are two types of oxygens: 3 O_A oxygens closest to the TMI and 3 O_B at a longer distance. Geometry optimizations were performed with density functional theory using the Amsterdam Density Functional (ADF) or the turbomole code. Two functionals were considered: BP86 and B3LYP. The results for the $\text{CuO}_6\text{Si}_4\text{Al}_2(\text{OH})_{12}$ and $\text{CoO}_6\text{Si}_4\text{Al}_2(\text{OH})_{12}$ clusters are shown in Table IV.10. Both for Co^{2+} and for Cu^{2+} the primary coordination sphere is constructed with the three O_A oxygens and one O_B oxygen. The latter is the oxygen connecting an Al tetrahedron with a Si tetrahedron. The same holds, if only one Al tetrahedron is present in the sixring, but not with three Al tetrahedra or no Al tetrahedra at all.

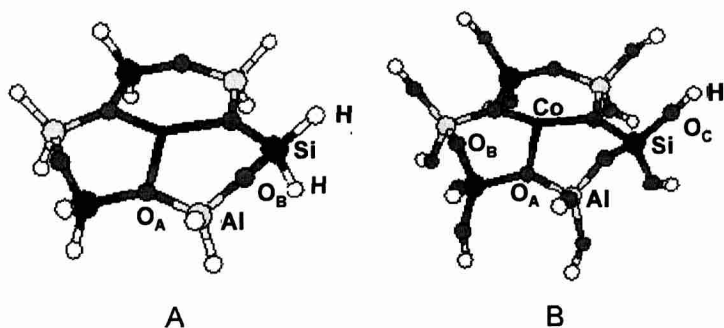


Figure IV.41. The sixring site modelled with the clusters $\text{CoO}_6\text{Si}_{6-x}\text{Al}_x\text{H}_{12}^{(2-x)+}$ (A) and $\text{CoO}_6\text{Si}_{6-x}\text{Al}_x(\text{OH})_{12}^{(2-x)+}$ (B) (American Chemical Society, Copyright 1998).

Table IV.10. Results of the geometry optimizations of the cluster models $\text{CuO}_6\text{Si}_4\text{Al}_2(\text{OH})_{12}$ and $\text{CoO}_6\text{Si}_4\text{Al}_2(\text{OH})_{12}$.

	$\text{CuO}_6\text{Si}_4\text{Al}_2(\text{OH})_{12}$	$\text{CoO}_6\text{Si}_4\text{Al}_2(\text{OH})_{12}$
$\text{R}(\text{Cu}-\text{O}_{\text{A}1})$ (Å)	1.90	1.91
$\text{R}(\text{Cu}-\text{O}_{\text{A}2})$ (Å)	2.08	2.02
$\text{R}(\text{Cu}-\text{O}_{\text{A}3})$ (Å)	2.01	2.09
$\text{R}(\text{Cu}-\text{O}_{\text{B}1})$ (Å)	3.31	3.25
$\text{R}(\text{Cu}-\text{O}_{\text{B}2})$ (Å)	2.19	2.35
$\text{R}(\text{Cu}-\text{O}_{\text{B}3})$ (Å)	3.30	3.00
$\text{O}_{\text{A}1}-\text{Cu}-\text{O}_{\text{A}2}$ (°)	109.9	116.1
$\text{O}_{\text{A}1}-\text{Cu}-\text{O}_{\text{A}3}$ (°)	143.1	131.7
$\text{O}_{\text{A}2}-\text{Cu}-\text{O}_{\text{A}3}$ (°)	105.7	105.7

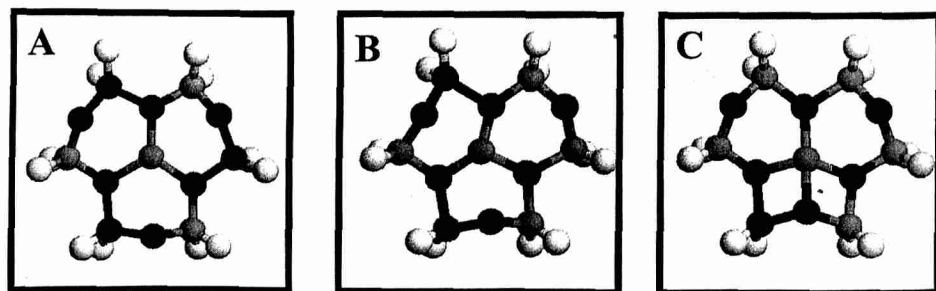


Figure IV.42. The sixring site modelled with cluster $\text{CoO}_6\text{Si}_{6-x}\text{Al}_x(\text{H})_{12}^{(2-x)+}$ as a function of the Al content : (A) 3 Al; (B) 2Al and (C) 1 Al.

The following happens upon coordination of a TMI to a sixring site. The TMI tries to maximize its coordination number. This is schematically illustrated in Figure IV.42 for cluster $\text{CoO}_6\text{Si}_{6-x}\text{Al}_x(\text{H})_{12}^{(2-x)+}$ with different Al-contents. It takes the three O_A atoms in its primary coordination sphere and one or two supplementary O_B oxygens. The latter is only possible if the sixring is asymmetric. Thus, one (Figure IV.42C) or two (Figure IV.42B) Al tetrahedra must be present.

Table IV.11. Electronic spectra of the $\text{CuO}_6\text{Si}_4\text{Al}_2(\text{OH})_{12}$ and $\text{CoO}_6\text{Si}_4\text{Al}_2(\text{OH})_{12}$ models calculated using the CASPT2 method.

Calculated excitation energies (cm^{-1})	$\text{CuO}_6\text{Si}_4\text{Al}_2(\text{OH})_{12}$	$\text{CoO}_6\text{Si}_4\text{Al}_2(\text{OH})_{12}$
	7828	6239
	10141	15881
	10827	16492
	14575	25243

The electronic spectra of the models were calculated with the CASPT2 method (MOLCAS software) and the results are given in Table IV.11. There is excellent agreement between experimental (Figure IV.40) and calculated (Table IV.11) spectra in terms of general frequency range of the transitions. The fine structure of the experimental spectra is not fully recovered. There are two reasons for this:

- (a) The experimental spectra are a superposition of spectra of Cu^{2+} or Co^{2+} on sixrings with one, two or three Al tetrahedra. They give rise to similar spectra with slightly different band positions.
- (b) Spin orbit coupling has been neglected in the calculations.

The lesson to be learned from this study is that TMI induce strong local distortions in surface sites, because they try to maximize their coordination number. These local distortions can be realized if one or two Al atoms substitute Si in the tetrahedra. The next step is of course to study the effect of these local distortions on the chemistry of the TMI.

An obvious problem with the analysis of DRS spectra of dehydrated TMI-zeolites is that TMI will simultaneously occupy different cation sites. The corresponding spectroscopic measurements yield spectra, which are a superposition of spectra of the TMI on each site. From these overlapping spectra it is very difficult to separate the various components or fingerprint spectra. One usually relies on the detailed spectroscopic analysis of series of spectra, obtained by variation of one variable at a time; e.g., TMI-loading. An example of such a series of spectra is given in Figure IV.43 for dehydrated Co^{2+} -exchanged zeolite A. A convenient way to analyze the spectra is by using chemometrics. As was discussed above, this is a beautiful approach because it is – in principle – an unbiased analysis. The results of the analysis are shown in Figure IV.43. Two (zeolite A) or three (X- and Y-type zeolites) components were obtained, which were ascribed to octahedral Co^{2+} in site

I, trigonal Co^{2+} in sixring sites and pseudo-tetrahedral Co^{2+} in sixring sites [43]. In the latter case an extra-framework oxygen is in the primary coordination sphere, presumably coming from a residual water molecule.

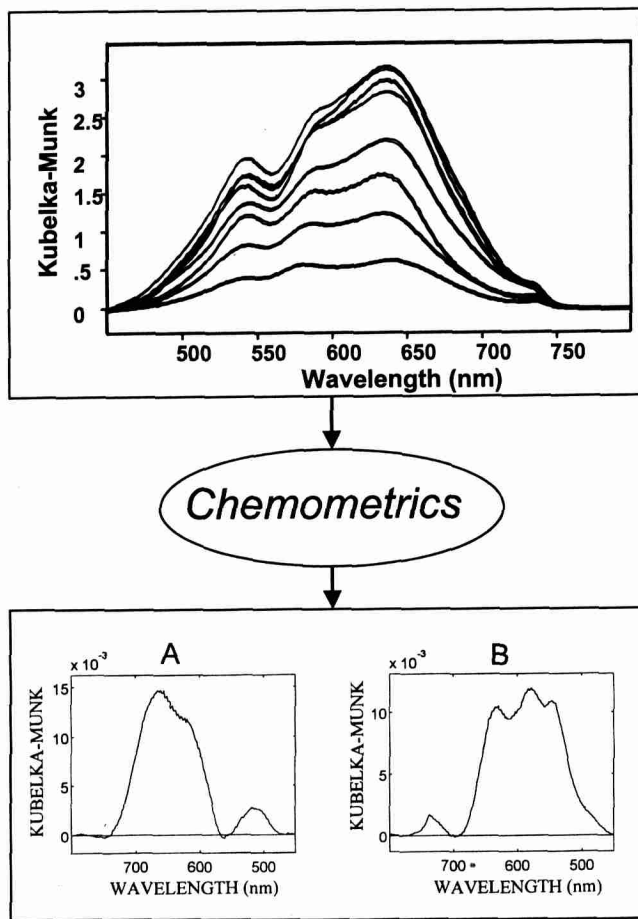


Figure IV.43. DRS spectra of dehydrated Co^{2+} -exchanged zeolite A as function of the Co-content, and the obtained pure components as revealed by the SIMPLISMA analysis.

As the progress in spectroscopic techniques continues, researchers can obtain more and more data in shorter and shorter time spans, and the need for efficient methods of data handling and data analysis increases. There are also drawbacks. The most important has to do with the dataset. If the individual components of the overall spectra have very different fingerprint spectra with clearly separated band positions, then these fingerprint spectra will be easily extracted from the overall dataset by chemometrics. Another point of attention is the extent of the dataset. A minimum number of spectra are necessary, and the statistically required number increases with

the number of unknowns which are in the dataset. It is not always possible to obtain such a large homogeneous dataset of spectra on a particular series of samples. A minimum of eight Co-samples with different Co content had to be prepared for the analysis of the spectra of Figure IV.43.

Co²⁺-ions occupy at least three sites after calcination: site I, site I' and site II in faujasite-type zeolites (see Figure IV.39). The question one can ask now is if the site occupancies are independent of the temperature or whether they are temperature dependent. It is indeed expected that at high temperature Co²⁺ migrates to the sites, which provide the highest coordination number. This is site I with pseudo-octahedral coordination. The condition is that the mobility of Co²⁺ should be high enough to measure this change of coordination in a reasonable time span. The *in situ* DRS spectra of Co²⁺ in calcined zeolite Y are shown in Figure IV.44 [41].

One clearly observes the expected band intensity increase upon cooling the sample from 500°C to 100°C. This is due to a combination of reduction of the background signal and resiting of Co²⁺. The latter becomes prominent upon cooling from 100°C to 25°C by the complete change in relative band intensities. The process continues over a long time period, because upon leaving the sample at room temperature the spectrum continues to change. A detailed analysis of these spectra in terms of siting of Co²⁺ has not yet been made. In order to do that, fingerprint spectra of Co²⁺ at the different sites, which come into play, are necessary. So far, only the sixring site has been thoroughly characterized both experimentally and theoretically.

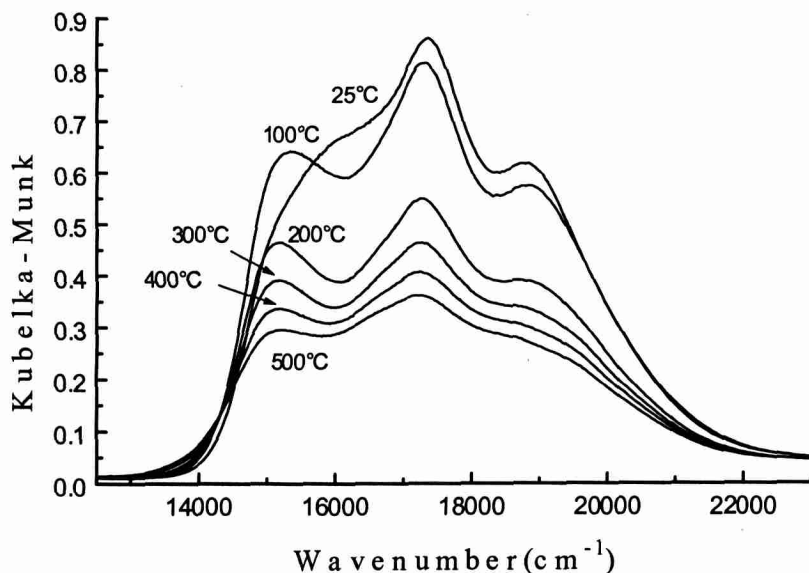


Figure IV.44. *In situ* DRS spectra of Co²⁺ in calcined zeolite Y as function of the temperature.

4.4. Concluding Remarks

DRS in the UV-VIS-NIR region is a well-established spectroscopic technique, which is based on known and easily accessible theories, such as crystal field, ligand field and molecular orbital theory. This makes the interpretation of the DRS spectra relatively easy, whereas band decomposition routines and chemometrical techniques assist the user in a more detailed and quantitative analysis of the DRS spectra. Indeed, the existence of broad and overlapping absorption bands may often lead to biased analysis. It is also clear that the DRS technique can be applied at different levels of sophistication: from merely detecting the presence of a certain oxidation state of a supported TMI up to a detailed distribution of different oxidation states and coordination environments under catalytic conditions. The use and further development of *in situ* capabilities is of paramount importance because only then it will become possible to identify the catalytic active site, and to develop relevant structure-activity/selectivity relationships in the field of heterogeneous catalysis.

We have also learnt in this chapter that the support characteristics have a tremendous impact on the properties of TMI on surfaces. For example, it has been shown that both the molecular structure and redox behavior of supported chromium oxides are determined by the $\text{SiO}_2:\text{Al}_2\text{O}_3$ ratio of the support. The reverse is, however, also true. TMI, such as Co^{2+} and Cu^{2+} , can induce strong local distortions in the surface because of their tendency to maximize their coordination sphere.

Finally, it is important to stress that the number of quantitative DRS studies is still very limited, and we hope that more quantitative studies on supported metal oxide catalysts will appear in the literature. Only by a systematic and intelligent application of the DRS technique, in conjunction with mathematical and statistical routines, can all the necessary information be extracted and fully appreciated.

4.5. References

- [1] G. Kortüm, Reflectance spectroscopy, Springer-Verlag, Berlin, 1969.
- [2] R.A. Schoonheydt, Characterization of Catalysts, F. Delannay (Ed.), Marcel Dekker, 1984, p. 125.
- [3] R. Kellerman, Spectroscopy in Heterogeneous Catalysis, W.N. Delgass, G.L. Haller, R. Kellerman and J.H. Lunsford (Eds.), Academic Press, New York, 1979, p. 86.
- [4] K. Klier, Vibrational Spectroscopies for Adsorbed Species, A.T. Bell and M.L. Hair (Eds.), ACS Symp. Ser. 1980, 137, 141.
- [5] R.A. Schoonheydt, Advanced Methods in Clay Minerals Analysis, J.J. Fripiat (Ed.), Elsevier, Amsterdam, 1981, p. 169.
- [6] K. Klier, J.Opt.Soc.Am., 1972, 62, 882.
- [7] B.M. Weckhuysen and R.A. Schoonheydt, Catal. Today, 1999, 49, 441.

- [8] Optical Spectroscopy: Sampling Techniques Manual. Harric Scientific Corporation, New York, 1987.
- [9] N.N. Greenwood and A. Earnshaw, Chemistry of the Elements, Pergamon Press, Oxford, 1984.
- [10] R.G. Burns, Mineral Applications of Crystal Field Theory, Cambridge University Press, Cambridge, 2nd Ed., 1993.
- [11] D.F. Shriver, P.W. Atkins and C.H. Langford, Inorganic Chemistry, Oxford University Press, Oxford, 1992.
- [12] Y. Tanabe and S. Sugano, J. Phys. Soc. Japan, 1954, 9, 753.
- [13] Z.G. Szabo, K. Kamaras, S. Szebini and I. Ruff, Spectrochimica Acta, 1978, 34a, 607.
- [14] B.M. Weckhuysen, I.E. Wachs and R.A. Schoonheydt, Chem. Rev., 1996, 96, 3327; B.M. Weckhuysen, L.M. De Ridder and R.A. Schoonheydt, J. Phys. Chem., 1993, 97, 4756; B.M. Weckhuysen, A.A. Verberckmoes, A.L. Buttiens and R.A. Schoonheydt, J. Phys. Chem., 1994, 98, 579; B.M. Weckhuysen, L.M. De Ridder, P.J. Grobet and R.A. Schoonheydt, J. Phys. Chem. 1995, 99, 320.
- [15] B.M. Weckhuysen, R.A. Schoonheydt, J.M. Jehng, I.E. Wachs, S.J. Cho, R. Ryoo, S. Kijlstra and E. Poels, J. Chem. Soc. Faraday Trans., 1995, 91, 3245.
- [16] A. Bensalem, B.M. Weckhuysen and R.A. Schoonheydt, J. Phys. Chem. B, 1997, 101, 2834.
- [17] G. Catana, R.R. Rao, B.M. Weckhuysen, P. Van Der Voort, E.F. Vansant and R.A. Schoonheydt, J. Phys. Chem. B, 1998, 102, 8005.
- [18] B.M. Weckhuysen, H.J. Spooen and R.A. Schoonheydt, Zeolites, 1994, 14, 450.
- [19] D.L. Massart, S.N. Vandeginste, Y. De Ming, Y. Michotte and L. Kaufmann, Chemometrics: A textbook, Elsevier, Amsterdam, 1988.
- [20] S. Wold, Chem. Int. Lab. Syst. 1987, 2, 37.
- [21] P. Geladi and B.R. Kowalski, Anal. Chim. Acta, 1986, 185, 1.
- [22] M.J. Adams, Chemometrics in Analytical Spectroscopy, The Royal Society of Chemistry, Cambridge, 1995.
- [23] W. Windig and J. Guilment, Anal. Chem., 1991, 63, 1425.
- [24] W. Windig, C.E. Heckler, F.A. Agblevor and R.J. Evans, Chem. Int. Lab. Syst. 1992, 14, 195.
- [25] W. Windig and D.A. Stephenson, Anal. Chem., 1992, 64, 2735.
- [26] B.M. Weckhuysen, A.A. Verberckmoes, A.R. De Baets and R.A. Schoonheydt, J. Catal., 1997, 166, 160.
- [27] B.M. Weckhuysen and R.A. Schoonheydt, Catal. Today, 1999, 51, 223.
- [28] B.M. Weckhuysen, A.A. Verberckmoes, J. Debaere, K. Ooms, I. Langhans and R.A. Schoonheydt, J. Mol. Catal., 2000, 151, 115. B.M. Weckhuysen, A. Bensalem and R.A. Schoonheydt, J. Chem. Soc. Faraday Trans., 1998, 94, 2011.
- [29] A.A. Verberckmoes, B.M. Weckhuysen and R.A. Schoonheydt, Micropor. Mesoporous Materials, 1998, 22, 165.

- [30] B.M. Weckhuysen, R.R. Rao, J.A. Martens and R.A. Schoonheydt, *Eur. J. Inorg. Chem.*, 1999, 565.
- [31] Q. Gao, B.M. Weckhuysen and R.A. Schoonheydt, *Micropor. Mesoporous Materials*, 1999, 27, 75.
- [32] B.M. Weckhuysen and R.A. Schoonheydt, *Zeolites*, 1994, 14, 360.
- [33] B.M. Weckhuysen, I.P. Vannijvel and R.A. Schoonheydt, *Zeolites*, 1995, 15, 482.
- [34] B.M. Weckhuysen, A.A. Verberckmoes, I.P. Vannijvel, J.A. Pelgrims, P.L. Buskens, P.A. Jacobs and R.A. Schoonheydt, *Angew. Chem., Int. Ed.* 1995, 107, 2868.
- [35] B.M. Weckhuysen, A.A. Verberckmoes, L. Fu and R.A. Schoonheydt, *J. Phys. Chem.* 1996, 100, 9456.
- [36] L. Fu, B.M. Weckhuysen, A.A. Verberckmoes and R.A. Schoonheydt, *Clay Minerals*, 1996, 31, 491.
- [37] D. Goldfarb, Y. Gao, P. Manikandan, T. Shane, B.M. Weckhuysen, H. Leeman and R.A. Schoonheydt, submitted for publication.
- [38] W.J. Mortier, *Compilation of extra-framework sites in zeolites*, Butterworths, Guildford, 1992.
- [39] K. Klier and H. Ralek, *J. Phys. Chem. Solids*, 1968, 29, 951; K. Klier and V. Cerny, *J. Phys. Chem. Solids*, 1968, 29, 945; R. Polak and K. Klier, *J. Phys. Chem. Solids*, 1969, 30, 2231; D. Packet and R.A. Schoonheydt, *Proc. 7th Int. Zeolite Conf.*, Y. Murakami, A. Iijima and J.W. Ward (Eds.), Kodansha, Tokyo, 1986, p.385.
- [40] K. Klier, P.J. Dutta and R. Kellerman, *ACS Symp. Ser.*, 1977, 40, 108; K. Klier, *Langmuir*, 1988, 4, 13; D. Packet and R.A. Schoonheydt, *ACS Symp. Ser.*, 1988, 368, 203; R.A. Schoonheydt, *Catal. Rev. Sci. Eng.*, 1993, 35, 129.
- [41] A. Verberckmoes, *Coordination of Cobalt in Zeolites: Spectroscopy and Theory*. Ph.D. thesis, K.U.Leuven, 1998; A.A. Verberckmoes, R.A. Schoonheydt, A. Ceulemans, A. Delabie and K. Pierloot, *Proceedings of the 12th International Zeolite Conference*, Materials Research Society Proceedings, M.M.J. Treacy, B.K. Marcus, M.E. Bisher and J.B. Higgins (Eds.), 1999, p. 387.
- [42] K. Pierloot, A. Delabie, C. Ribbing, A.A. Verberckmoes and R.A. Schoonheydt, *J. Phys. Chem.B*, 1998, 102, 10789.
- [43] A.A. Verberckmoes, B.M. Weckhuysen, J. Pelgrims and R.A. Schoonheydt, *J. Phys. Chem.*, 1995, 99, 15222; A.A. Verberckmoes, B.M. Weckhuysen, R.A. Schoonheydt, K. Ooms and I. Langhans, *Anal. Chim. Acta*, 1997, 348, 267.